

Accepted to ApJ

Identification of an Extended Accretion Disk Corona in the Hercules X-1 Low State: Moderate Optical Depth, Precise Density Determination, and Verification of CNO Abundances

M. A. Jimenez-Garate

MIT Center for Space Research, 70 Vassar St (NE80-6009), Cambridge, MA 02139

`mario@space.mit.edu`

J. C. Raymond

Center for Astrophysics, 60 Garden St., Cambridge, MA 02138

`raymond@cfa.harvard.edu`

D. A. Liedahl

Lawrence Livermore National Laboratory, Department of Physics and Advanced Technologies, 7000 East Ave., L-41, Livermore, CA 94550

`liedahl1@llnl.gov`

and

C. J. Hailey

Columbia Astrophysics Laboratory, 538 W. 120th St., New York, NY, 10027

`chuckh@astro.columbia.edu`

ABSTRACT

We identify an accretion disk atmosphere and corona from the high resolution X-ray spectrum of Hercules X-1, and we determine its detailed physical properties. More than two dozen recombination emission lines (from Fe XXVI at 1.78 Å to N VI at 29.08 Å) and Fe K α , K β fluorescence lines were detected in a 50 ks observation with the *Chandra* High-Energy Transmission Grating Spectrometer (HETGS). They allow us to measure the density ($n_e = 2 \pm 1 \times 10^{13}$ cm from Mg XI), temperature ($kT = 7 \pm 3$ eV from Ne IX), spatial distribution, elemental composition, and kinematics ($\Delta v \lesssim 260$ km s $^{-1}$) of the plasma. We exclude HZ Her as the source of the recombination emission. We compare accretion disk model atmospheres with the observed spectrum in order to constrain the stratification of density and ionization, elemental composition, energetics, and thermal stability. The derived disk atmosphere and corona radii are $8 \times 10^{10} \lesssim r \lesssim 1 \times 10^{11}$ cm, in agreement with previously measured eclipse ingress light curves. The atmospheric spectrum observed during the low state is photoionized by the main-on X-ray continuum, indicating that the disk is observed edge-on during the low state. We infer the mean number of scatterings $\langle N \rangle$ of Ly α and Ly β line photons from H-like ions. We derive $\langle N \rangle \lesssim 69$ for O VIII Ly α_1 , which rules out the presence of a mechanism modeled by Sako (2003) to enhance N VII emission via

a line overlap with O VIII. The line optical depth diagnostics are consistent with a flattened atmosphere. Our spectral analysis, the disk atmosphere model, and the presence of intense N VII and N VI lines (plus N V in the UV), confirm the over-abundance of nitrogen relative to other metals, which was shown to be indicative of CNO cycle processing in a massive progenitor. The spectral signatures of a thermal instability in the photoionized plasma are not evident, but the measured density is in the stable regime of the models.

Subject headings: X-rays: binaries — line: formation — line: identification — pulsars: individual (Her X-1) — accretion, accretion disks — binaries: eclipsing

1. Introduction

High-resolution spectroscopic observations of X-ray binaries have shown in some cases the presence of extended X-ray emitting plasmas or outflows surrounding the accretion disk. The detection of these components and their kinematic properties has been made possible by the observation of emission or absorption lines from very highly ionized metals. In the case of Hercules X-1, a bright intermediate-mass X-ray binary with $P_{\text{orb}} = 1.7$ day orbital period and a $P_{\text{pulse}} = 1.24$ s X-ray pulsar (Tananbaum et al. 1972; Wilson, Scott, & Finger 1997), observations with the *XMM-Newton* Reflection Grating Spectrometer (RGS) showed a strong 35 d phase dependence in the high-resolution spectrum (Jimenez-Garate et al. 2002). The $P_{\Psi} \sim 35$ d pseudo-periodic cycle (Giacconi et al. 1973) has been associated with a tilted and precessing accretion disk (Petterson 1975; Petterson, Rothschild, & Gruber 1991; Scott, Leahy, & Wilson 2000). Through the 35 d cycle, the X-ray light-curve is asymmetric and contains two maxima: a state of ~ 8 d duration reaching the peak flux F_{max} named the *main-on*, and a secondary high state of ~ 4 d duration reaching $\sim 1/3 F_{\text{max}}$ named the *short-on*. A *low state* with $\sim 1/20 F_{\text{max}}$ ensues at other epochs. The main-on spectrum exhibits a strong continuum, with evidence for weak and very broad emission lines, while the low state shows bright and narrow emission lines dominating over a very weak continuum. The short-on is intermediate, with a moderate continuum flux and more intense emission lines than the low state (Jimenez-Garate et al. 2002). The Fe K α line follows a similar pattern. *XMM-Newton* EPIC data show a 6.4 keV Fe K α line which is practically unresolved during the low and short-on states, and a broad line at 6.5 keV with 330 ± 20 eV FWHM during the main-on (Ramsay et al. 2001). Matter close to the magnetosphere and the pulsar appears to be observable during the main-on only. This behavior supports the picture of a precessing accretion disk, since the spectroscopic appearance of the disk atmosphere and the pulsar should be highly dependent on inclination. Analysis of the RGS spectrum showed a clear over-abundance of N with respect to Ne, as well as a moderate under-abundance of O and C with respect to Ne. The N over-abundance was proposed as a signature of CNO cycle nucleosynthesis occurring at an early phase in the binary system, and it is indicative of a star twice or more times more massive than the secondary/companion (Jimenez-Garate et al. 2002). This is indicative of a massive progenitor of the system and a period of extreme mass loss, as had been predicted by evolutionary models of LMXBs (Podsiadlowski, Rappaport, & Pfahl 2002). Sako (2003) suggested that the N over-abundance is not real, but that it is due instead to an X-ray Bowen fluorescence effect which occurs at large line optical depths. In this article, we quantify the relevant line optical depths to distinguish between the X-ray Bowen effect or the abundance anomaly scenarios.

Hercules X-1 has been observed extensively. Optical light-curves (Gerend & Boynton 1976) and X-ray eclipses (Tananbaum et al. 1972) yield a $P_{\text{orb}} = 1.7$ day orbital period. The $1.5 \pm 0.3 M_{\odot}$ neutron star has a $2.3 \pm 0.3 M_{\odot}$ companion, HZ Her, which changes from A to B spectral-type over the orbital period, due to the strong X-ray illumination on its surface (Reynolds et al. 1997). The unabsorbed luminosity of Her X-1 is

$L = 3.8 \times 10^{37}$ ergs $^{-1}$, using a distance of $D = 6.6 \pm 0.4$ kpc (Reynolds et al. 1997). The Her X-1 broadband X-ray spectrum during the main-on state consists of a blackbody component with temperature $kT \sim 90$ eV, plus a power-law component with a 24 keV exponential cutoff, and a 42 keV cyclotron feature (dal Fiume et al. 1998). The X-ray light-curve, the variations in the pulse profiles (Deeter et al. 1991), and the variability of the dips (Giacconi et al. 1973; Scott & Leahy 1999), are fit by a geometric model of a precessing, warped accretion disk, with an 85° inclination with respect to the line of sight, a 20° precession opening angle for the outermost disk, and an 11° precession angle for the innermost disk (Scott, Leahy, & Wilson 2000). The ultraviolet (UV) spectrum exhibits line emission from C V, N V, and O V, which have two separate velocity components. A narrow UV line component is thought to originate on the illuminated face of HZ Her. The broad UV line region likely originates in a prograde accretion disk of $\sim 10^{11}$ cm radius (Boroson et al. 2000). One of the questions to be resolved is whether the X-ray line emission has a similar origin to the UV. The broadening of the X-ray line emission indicates that it can originate at radii similar to the UV. For the case of an irradiated disk atmosphere, the UV line region is denser and deeper than the X-ray line region.

In this work, we interpret the broadband (1.5 Å to 30 Å) high-resolution X-ray spectrum of Her X-1 and investigate the nature of the line emitting region(s). The *Chandra* grating spectrum allows us to detect a wealth of spectral features which had not been previously observed in Her X-1. Our data reduction procedure is described in §2. To interpret the spectrum, we use two complementary approaches: 1) an analytic approach for constraining the physical parameters of the plasma, based solely on the photoionized plasma physics; and 2) a synthetic approach, by comparing the spectrum with that of an astrophysical model. In §3, discuss the origin of the Fe K α line and we perform spectral diagnostics on density, kinematics, and location from the recombination lines. In §4, we utilize standard photoionized plasma models and radiative recombination rates to perform an emission measure analysis, and to quantify the ionization distribution of the plasma, the emitting volume, and the ratios among the metal abundances. We also compare the model temperatures with those measured from radiative recombination continua (RRC). In §5, we quantify the mean number of scatterings of selected lines, which shows that the optical depth is not high enough for the X-ray Bowen fluorescence effect to take place in Her X-1. Line depth diagnostics also provide evidence for an anisotropic plasma distribution. In §6, we identify the nature of the X-ray emission region on the basis of a comparison of an accretion disk and corona model with the observed spectrum. In §7, we discuss the thermal stability of the plasma. Finally, in §8 we compare the Her X-1 spectrum with that of Accretion Disk Corona (ADC) sources, and we conclude in §9.

2. *Chandra* Observations

Hercules X-1 was observed on 2002 May 5 at 10:15 UT with the *Chandra* High Energy Transmission Grating Spectrometer (Canizares et al. 2000, HETGS). The observation lasted 49.4 ks. Data from the All-Sky Monitor (ASM) instrument onboard the Rossi X-ray Timing Explorer (RXTE), indicated that Her X-1 was in the low state ($\Psi = 0.44 - 0.46$) while at mid-orbit ($\phi = 0.33 - 0.67$) during the *Chandra* observation. From the RXTE ASM data, we determined that first main-on start signal immediately preceding the Chandra observation occurred on MJD 52384.22. Scott & Leahy (1999) observed that main-on turn-ons occur only orbital phases 0.23 or 0.68, possibly due to a disk-orbit locking mechanism. The closest, most likely main-on start time occurred at orbital phase 0.23, at MJD 52383.956, ~ 10 hr earlier than the RXTE ASM detection.

We processed the HETGS data with the CIAO analysis software version 3.0. We obtained Medium Energy Grating (MEG) and High Energy Grating (HEG) spectra, which have energy resolution FWHM of $\Delta\lambda = 0.023$ Å and $\Delta\lambda = 0.012$ Å, respectively. The ACIS-S CCD was set in FAINT mode since the low

state does not produce pile-up in the image, and this minimizes the background in the spectrum. We use the *destreak* tool to clean the ACIS-S image. The *mkrmf* and *mkarf* tools are used to produce the response matrices and effective area applicable to our observation. We use the calibration data CALDB version 2.26, which was updated 2004 Feb 2 to correct for the contamination layer on ACIS-S. We used the ISIS spectral analysis software in our model fitting and flux measurements (Houck & Denicola 2000). The *lightcurve* routine was used to extract the time variability of the flux. Her X-1 was placed at a Y Offset of 0.33 arcmin, which is practically on-axis.

3. Spectral Analysis

The HEG and MEG spectra of Her X-1 exhibit emission lines throughout the X-ray band. Together, the spectra exhibit bright lines from the H-like and He-like ions of N, O, Ne, Mg, and Si, plus the lines from H-like ions of S and Fe. The MEG and HEG counts spectra in Figure 1 show a strong Fe K α fluorescence line, as well as numerous recombination emission lines. The HEG spectrum in Figure 2 highlights the Fe K α line from low ionization states and a line from the high ionization state Fe XXVI. The spectra of HEG and MEG are added for display purposes in Figure 3, and the MEG spectrum at the high wavelength end is shown in Figure 4. The detection of RRCs, as well as the fact that weak Fe L lines are observed, are characteristic of photoionized plasmas (Liedahl & Paerels 1996; Liedahl 1999). We measure a 0.5–7 keV flux of $F_{0.5-7} = 3.3 \times 10^{-11} \text{ erg cm}^{-2} \text{ s}^{-1}$, and the fluxes of individual spectral features are listed in Table 1. We use Cash statistics to fit the individual spectral features and obtain the statistical errors. Continuum fit parameters are shown in Table 2.

3.1. Fe fluorescence

The data allow us to fit independently the K α_1 and K α_2 lines, which are merged in a single feature. We also detect the K β line. The measured Fe K fluorescence line energies, as well as the line ratios among K α_1 , K α_2 , and K β , all show that the iron is neutral, based on the Kaastra & Mewe (1993) calculations. The K α /K β ratio is 6.2 ± 1.6 (compared to 7.99 for Fe I from Kaastra & Mewe), while the K α_1 /K α_2 ratio is 2.28 ± 0.45 (compared to 2.00, *idem*). Any iron ion with an L-shell electron can fluoresce with high yields as well. However, the line energy observed corresponds to Fe I–Fe IX (Palmeri et al. 2003), and likely up to Fe XIII. We approximate the 6.4 keV fluorescence line flux (in $\text{ph cm}^{-2} \text{ s}^{-1}$) with

$$F \approx \frac{1}{2} Y_{\text{Fe}} f T \left(\frac{\Omega}{4\pi} \right) \int_{7.1 \text{ keV}}^{200 \text{ keV}} F_E (1 - e^{-\tau_{\text{Fe}}}) dE \quad (1)$$

where we take F_E to be the continuum flux (in $\text{ph cm}^{-2} \text{ s}^{-1} \text{ keV}^{-1}$) observed during the main-on by dal Fiume et al. (1998), τ_{Fe} is the optical depth of M-shell iron, $Y_{\text{Fe}} = 0.34$ is the fluorescence yield of Fe, Ω is the solid angle subtended by the fluorescing plasma from the vantage point of the X-ray pulsar, $0 < T < 1$ is a transmission coefficient due to absorption from species other than Fe I–Fe XIII and Compton scattering, and f is the fraction of the fluorescing region which is visible to us. Roughly half the fluorescent photons are emitted downward into the optically thick gas. The 0.1 to 100 keV continuum flux during the main-on is $\int F_E dE = 6.7 \times 10^{-9} \text{ erg cm}^{-2} \text{ s}^{-1}$, and it is taken from the Model 2 fit by dal Fiume et al. (1998), which consists of an absorbed blackbody plus broken power law, with an exponential cutoff and cyclotron absorption line. Using $\tau_{\text{Fe}} \sim 4$, which is an estimate of the depth from which an Fe K photon can escape, we obtain $fT\Omega \sim 0.22$. The solid angle subtended by the companion star is $\Omega \sim 0.50$, and the solid angle subtended by

the disk photosphere is $\Omega \sim 1.0$, as obtained from the illuminated disk model (Jimenez-Garate, Raymond, & Liedahl 2002). These Ω are quite similar. Both cases produce $fT \sim 0.2\text{--}0.4$. Given $0.33 < \phi < 0.67$ during the observations, we estimate that $f \sim 2/3$ of the illuminated star is visible. For the disk, $f \lesssim 1/2$ for the scenario of a self-shielding edge-on disk (see next section). In both cases reasonable transmission $T \gtrsim 0.5$ can be obtained. Thus, we need to employ the orbital variability to distinguish amongst these components (§3.4). The Fe K α fluorescence line flux and broadening are much larger during the main-on than during the short-on, and the low state line flux measured with *XMM-Newton*, of $(2\text{--}12) \times 10^{-4}$ ph cm $^{-2}$ s $^{-1}$ (Zane et al. 2004), brackets the Fe K α line flux we measure with HETGS (see Table 1).

3.2. Unbroadened Lines

The gratings do not resolve any Doppler width in the emission lines. The Doppler broadening $(\Delta v)_\sigma$ is measured by fitting Gaussian profiles to the brightest lines in the spectra, such that $(\Delta v)_{\text{FWHM}} \simeq 2.35(\Delta v)_\sigma$. Table 1 shows that the best upper limits on Δv are placed on the lines with largest λ . The observed line broadening is entirely attributed to their doublet nature. We set 90 % confidence limits of $(\Delta\lambda)_\sigma = 0\text{--}8$ mÅ for the O VII i line with MEG, $(\Delta\lambda)_\sigma = 8\text{--}17$ mÅ for the O VIII Ly α line with MEG, and $(\Delta\lambda)_\sigma = 0\text{--}3$ mÅ for the Ne IX i line with HEG. The remaining bright lines have similar $(\Delta\lambda)_\sigma$. The intrinsic line broadening, plus any residual instrumental broadening for MEG and HEG not accounted for in the response matrix, is quantified using the spectra of a bright star from which no velocity broadening is expected. We choose the star HR 1099 as reference, which yields $(\Delta\lambda)_\sigma = 4.8 \pm 0.4$ mÅ with HEG and $(\Delta\lambda)_\sigma = 5.2 \pm 0.6$ mÅ with MEG at 12.13 Å (99% confidence limits). By fitting a plasma model, we verify that this broadening can be fully accounted for by the Ne X Ly α -doublet, which is separated by 5 mÅ and should show a 2:1 intensity ratio. The doublet fully accounts for the measured $(\Delta\lambda)_\sigma$. Other lines in the HR 1099 spectrum are consistent with this. The upper limits on the velocity broadening on Table 1 are based on either the measured or reference $(\Delta\lambda)_\sigma$, whichever is largest. At the slightly lower resolving power of the *XMM-Newton* RGS, the short-on and low state emission lines of Her X-1 were unresolved (Jimenez-Garate et al. 2002).

The absence of a Doppler velocity broadening constrains the dynamics of the disk atmosphere and the geometry of the disk. Since the disk inclination is $i \sim 85^\circ$, the orbital velocity of the disk is given by $v \sim \sqrt{GM/R} \cos\Phi$, where G is the gravitational constant, M the neutron star mass, R the disk radius, and Φ is the azimuth on the disk. If the lines produced by a Φ -symmetric disk, translating the measured $(\Delta v)_\sigma$ into a physical size of the disk requires modeling the line profiles with a calculated (or assumed) emissivity versus radius. The disk lines would have double-peaked profiles. The profiles from a centrally illuminated disk of $10^{8.5} < r < 10^{11}$ cm radius in full view calculated with the Jimenez-Garate, Raymond, & Liedahl (2002) model can be fit with a $(\Delta v)_\sigma \sim 750$ km s $^{-1}$ Gaussian. Clearly the disk cannot be in full view in the Her X-1 low state. *This is an indication that we are observing the outer rim of the disk atmosphere and corona.* For a Φ -symmetric, edge-on, and optically thin disk, the emission region radius would be $r \gtrsim GM/[4(\Delta v)_\sigma^2]$. For the X-ray lines observed at highest resolving power, the inferred lower limits with this equation are $r \gtrsim (2\text{--}3) \times 10^{11}$ cm, larger than the neutron star Roche lobe and the disk size $r \sim 1.4 \times 10^{11}$ cm deduced from the eclipse ingress light curves of the He II, C IV, Si IV, and O V emission lines in the UV (Chiang 2001; Boroson et al. 2000). Therefore, the disk atmosphere is likely asymmetric. One interpretation is that due to the flared disk geometry, the disk shields itself, such that we only observe the far side of the disk, which causes the $\cos\Phi$ factor to reduce Δv . This does not require an asymmetric disk, just one that partially shields itself. Another interpretation is that the disk is asymmetric or warped, which can similarly reduce the observed Δv . Evidence of shielding in a warped disk was found by Chiang (2001)

in the UV emission line profiles. A third possibility is that the disk is Φ -symmetric, but has an atmosphere which is orbiting at sub-Keplerian velocities. The case of the asymmetric disk implies a modulation of the X-ray line fluxes with orbital phase (see §3.4).

3.3. A location and density diagnostic from He-like ions

The $\text{He}\alpha$ line triplets are shown in Fig. 5. At the HETGS resolution, each $\text{He}\alpha$ complex consists of the intercombination (i), forbidden (f), and resonance (r) lines. The He-like triplet diagnostics were performed with the *XMM-Newton* RGS spectrum for N VI, O VII, and Ne IX (Jimenez-Garate et al. 2002). Both RGS and HETGS spectra show that the $R = f/i$ flux ratio is zero for the latter ions. The HETGS spectrum reveals that the Mg XI and Si XIII $\text{He}\alpha$ lines behave differently: the R ratio is nonzero and increasing with Z (see Table 3). The value of the R ratio depends on the atomic kinetics in each ion. The f line can get converted into the i line by a process in which the metastable $1s2s\ 3S_1$ level is excited to $1s2p\ 3P_{1,2}$ (Porquet & Dubau 2000). This occurs when the excitation rate $w_{f \rightarrow i}$ is larger than the decay rate w_f of $1s2s\ 3S_1$ to the ground state. We note that the particular $1s2s\ 3S_1 \rightarrow 1s2p\ 3P_2$ transition does not modify the R ratio for the low and mid- Z ions, for which $1s2p\ 3P_2$ decays back quickly to $1s2s\ 3S_1$, instead of decaying to the ground state. An $R \sim 0$ ratio can be produced by either collisional excitation above a critical electron density n_e^{crit} (Porquet & Dubau 2000; Bautista & Kallman 2000) or by photoexcitation above a critical UV-photon flux F_{ν}^{crit} (Mewe & Schrijver 1978). We discuss both as limiting cases for which $R \rightarrow 0$. If both the plasma density and the ambient UV flux are below their thresholds, the R ratio reaches an asymptotic value of $R \gtrsim 2.2$, which increases with T and depends weakly on Z . For Mg XI at $T = 3 \times 10^5$ K, the maximum $R = 2.8$ (Porquet & Dubau 2000).

We first discuss the limiting case in which the density is below threshold and the UV flux is above threshold. From the measured UV flux F_{ν} , we constrain the distance (d) between the X-ray line emission region and the UV source. The dominant source of UV flux is the surface of the companion (see below). A similar diagnostic was used by Kahn et al. (2001). Jimenez-Garate et al. (2002) set a limit of $d < 7 \times 10^{11}$ cm for Her X-1. With the newly detected lines, d is shown to be equal or larger than the binary separation. To measure d , we quantify the photoexcitation rate by using the UV fluxes that were observed with the Hubble Space Telescope (*HST*) and the Far Ultraviolet Spectroscopic Explorer or FUSE (Boroson et al. 1996, 2000, 2001), and with the Hopkins Ultraviolet Telescope (Boroson et al. 1997). The relevant photoexcitation rate is:

$$w_{f \rightarrow i} = \frac{\pi e^2}{m_e c} F_{\nu_{f \rightarrow i}} f_{\text{osc}}, \quad (2)$$

where e , m_e are the electron charge and mass, c is the speed of light, f_{osc} is the oscillator strength, and $F_{\nu_{f \rightarrow i}}$ is the flux (in photons $\text{s}^{-1} \text{cm}^{-2} \text{Hz}^{-1}$) at frequencies resonant with the $1s2s\ 3S_1 \rightarrow 1s2p\ 3P_1$ transition in the UV. We use the f_{osc} calculated with the HULLAC atomic code (Klapisch et al. 1977), and those calculated by Cann & Thakkar (1992). Since $F_{\nu_{f \rightarrow i}}$ is a function of d , we constrain d by relating $w_{f \rightarrow i}$ to w_f .

In the second limiting case, the UV flux is below threshold and the density is above threshold. In this case, the lower limit of n_e can be obtained from the upper limit on R using the Porquet & Dubau (2000) calculations. The d calculated with Eqs. 2 and 3 in the first limiting case, as well as the inferred n_e in the second limiting case, are shown in Table 3.

A valuable new constraint is inferred from the Mg XI $\text{He}\alpha$ lines, which show a critical R ratio, that is, the value of $R = 0.52 \pm 0.13$ is intermediate between the asymptotic values of $R = 0.0$ and $R = 2.8$. The

measured R ratio implies that

$$w_{f \rightarrow i} \sim w_f. \quad (3)$$

For He-like ions other than Mg XI, Eq. 3 becomes an inequality. We interpret the Mg XI R ratio in two limits and in the general case. In the low density limit, the UV flux is at a critical value, and F_ν is measured. In the low F_ν limit, the density is at a critical value, and the measurement of n_e is applicable. In the general case, the same numbers for Mg XI become a lower limit for d and an upper limit for n_e . A confidence region in (d, n_e) space requires new atomic kinetics calculations. Since in the general case $d \geq 2 \times 10^{11}$ cm, we conclude that *the X-ray recombination line emission cannot possibly originate in the illuminated atmosphere of HZ Her*. This does not preclude an Fe K α fluorescence line to be produced on HZ Her. If the recombination lines did originate within the strong UV field of the companion, the Mg XI and Si XIII would have shown no f line and a strong i line, like the rest of the He-like ions. The caveat for the d -limits is the possibility that the UV from HZ Her are shielded on their way to the X-ray emission region, but not on their way to our line of sight. The 864 Å photons which photoexcite Si XIII are particularly vulnerable since they are above the Lyman edge. Such a shielding material could be the accretion disk itself, in which case the origin of the recombination lines in the disk atmosphere would be proven as well. Previously, no distinction could be made between the case of disk coronal emission and emission from the illuminated companion (Jimenez-Garate et al. 2002).

We base our arguments above in the fact that the primary source of UV emission in the binary system is HZ Her and not the accretion disk. This is known from the orbital phase variability. The UV continuum increases gradually from $\phi \sim 0.2$ until it peaks at orbital phase $\phi \sim 0.5$, and then decreases gradually until the illuminated face of HZ Her comes out of view at $\phi \sim 0.9$ (Boroson et al. 2000). The intermediate mass ($\sim 2.3 M_\odot$) and size of HZ Her causes it to produce copious UV emission by reprocessing of the neutron star X-rays. The accretion disk emission in the 1260–1630 Å band, which is identifiable from eclipse ingresses and egresses at $\phi = \pm 0.1$, represents a small fraction ($\sim 1/10$ to $1/20$) of the peak HZ Her emission at that band (Boroson et al. 2000). However, the question remains of how much UV continuum from the disk is visible to the disk atmosphere. Although the observed UV from the disk is fainter than that from the companion, that is partly because the disk is seen edge-on.

In sum, the weakening of any photoexcitation effects in the R ratios in Mg XI and Si XIII places a lower limit on the distance from HZ Her to the X-ray emitting region, or a requirement on shielding from the UV. These limits show that the X-ray lines are not produced on the illuminated surface of the companion, but instead arise in a high density region that is likely associated with the accretion disk.

3.4. Search for orbital variability

The X-ray light curve is flat at mid-orbit. The light curves for the total and Fe K α line fluxes are shown in Figure 6. A Bayesian block analysis (Scargle 2003) on these light curves showed no deviations from constant flux with 99.9% confidence. The coverage is limited to 1/3 of the orbit, so we cannot entirely rule out orbital variability in the spectrum. After all, Her X-1 exhibits eclipses in the low state (Scott & Leahy 1999). Clearly, the variability of the Her X-1 emission is distinct from that observed in the ADC source 4U 1822-37, the latter likely arising on an illuminated disk bulge (Cottam et al. 2001). The UV continuum emission from HZ Her shows a $\sim 25\%$ flux variation from $\phi = 0.5$ to $\phi = 0.65$, peaking at mid-orbit, and the lines of O V and N VI decrease in strength $\Delta\phi = 0.2$ away from eclipses (Boroson et al. 2000). With better phase coverage than ours, *XMM-Newton* UV flux and Fe K α flux measurements show a clear orbital modulation (Zane et al. 2004, see their Fig. 9), which suggests that at least some of the Fe K α flux originates

on the face of the companion. Our data show that the Fe K α flux was unusually flat during our observation.

4. XSTAR Photoionized Plasma Models and Emission Measure

The differential emission measure (DEM) maps the ionization distribution of the plasma. It serves as a basis for testing astrophysical emission models and measuring elemental abundance ratios. A DEM analysis is valid insofar as the spectrum is dominated by recombination emission, which occurs when the optical depth is such that the plasma does not destroy or enhance the lines above their recombination values. The luminosity of a line from level u to level l is given by

$$dL_{ul} = n_e n_{z,i+1} E_{ul} \eta_{ul} \alpha_{RR} dV \quad (4)$$

where $n_{z,i+1}$ is the number density of an ion with atomic number Z and charge $+(i+1)$, E_{ul} is the transition energy, dV is the differential volume, $\alpha_{RR} = \alpha_{RR}(T)$ is the total radiative recombination rate in units of $\text{cm}^3 \text{ s}^{-1}$, and η_{ul} is the fraction of all the recombination photons that produce line emission through the transition $u \rightarrow l$. This can be related to the $DEM = \int d(EM)/d(\log \xi)$ through the $d(EM) = n_e^2 dV$ available at each $\log \xi$, since:

$$dL_{ul} = \frac{n_{z,i+1}}{n_e} E_{ul} \eta_{ul} \alpha_{RR} d(EM) = \frac{n_{z,i+1}}{n_e} E_{ul} S_{ul} d(EM) \quad (5)$$

where the ionic density $n_{z,i+1} = A_Z n_H f_{i+1}$ is often expressed in terms of the elemental abundance A_Z , the proton density n_H , and the charge state fraction of the recombining ion f_{i+1} . The specific line power is defined as $S_{ul} = \eta_{ul} \alpha_{RR}$. Thus, the total line luminosity is

$$L_{ul} = \frac{A_Z n_H}{n_e} E_{ul} \int f_{i+1} S_{ul} \frac{d(EM)}{d(\log \xi)} d(\log \xi) \quad (6)$$

This sort of DEM procedure was illustrated by Liedahl (1999) and applied by Sako, Liedahl, Kahn, & Paerels (1999), and it is analogous to what has been used in collisionally ionized plasmas as $d(EM)/dT$ (Kaastra et al. 1996).

In the simplest analysis, we estimate the total emission measure $EM = \int n_e^2 dV$ for each ion, assuming each is formed at a single ξ_o and T_o . The EM for every prominent line in the spectrum is shown in Figure 7, calculated with the Solar abundances from Grevesse & Sauval (1998), with the updated C and O values from Allende Prieto, Lambert, & Asplund (2002). We estimate the elemental abundance ratios by enforcing the continuity of the EM as a function of ξ_o . The N VII and N VI line fluxes show a N over-abundance with respect to C, O, Ne, Mg, Si, S, and Fe. The C VI line flux is obtained from the *XMM-Newton* RGS spectra obtained by Jimenez-Garate et al. (2002). From Equation 6, it is useful to adopt $\epsilon \equiv f_{i+1} S_{ul}$ (in units of photons $\text{cm}^3 \text{ s}^{-1}$) as a measure of the line emissivity from now on. This ϵ is a function of ξ . We calculate the f_{i+1} in a grid of models with $0.0 < \log \xi < 5.0$ and $\Delta \xi = 0.1$, using XSTAR (Kallman & McCray 1982). We use the main-on spectrum as the ionizing continuum. The S_{ul} are calculated with HULLAC (Klapisch et al. 1977). The $\log T_o$ and $\log \xi_o$ of formation for the Ly α or He α lines are defined as the average values of $\log T$ and $\log \xi$ weighted by ϵ . The XSTAR/HULLAC model temperatures of formation span $32,500 \text{ K} < T_o < 6.7 \times 10^6 \text{ K}$, for N VI through Fe XXVI, respectively. We calculate the recombination rate at a single ξ_o and assume $f_{i+1} = 0.25$. We use $f_{i+1} = 0.25$ because the $\log \xi$ -averaged, emissivity-weighted value of f_{i+1} is approximately equal to that value. While this is just an approximation, it is more realistic than simply setting $f_{i+1} = 1$. The EM analysis in Figure 7 has the advantages of being simple and of making

the result independent of the plasma models; however, one sacrifices the accuracy of the EM distribution with ξ .

In principle, a more accurate analysis than the above is obtained with $DEM = d(EM)/d(\log \xi)$, by assuming that the DEM is constant in the ξ range at which each ion is formed. Again, we enforce continuity of the DEM as a function of ξ . We use the aforementioned Solar abundances. Figure 8 shows that the N abundance has a large excess, C is moderately depleted, and O is near the Solar value. A recalculation of the DEM with the Wilms, Allen, & McCray (2000) Solar abundances establishes that the N excess is just as large, while both the C and O depletion appear significant. This stems from the fact that the Wilms et al. abundances for both C and O are larger than Allende Prieto et al.’s by $\sim 62\%$ and $\sim 74\%$, respectively. The abundance pattern, and especially the N abundance, is clearly a signature of CNO cycle products, as shown previously by the *XMM-Newton* RGS spectral analysis, where the DEM was parameterized as a power-law and the Wilms et al. abundances were used (Jimenez-Garate et al. 2002). The uncertainties in the Solar abundances do not affect this conclusion, since no significant O depletion is needed. The CNO process consists of the rapid conversion of C to N and the 10^3 times slower conversion of O to N (Clayton 1983, and references therein). Evolutionary models of $2\text{--}12 M_\odot$ stars produce an increase in the N abundance by factors of a few, with C depletion in the tens of percent and O depletion of a few percent or less, after the H-burning phase is over (Schaller, Schaerer, Meynet, & Maeder 1992). Clearly the most noticeable signature will be the N abundance. It can be seen in the DEM that the abundance ratios among Ne, Mg, Si, S, and Fe are close to the Solar values. Figure 8 shows that successive pairs of the H-like and He-like ions of a given element indicate that the DEM decreases with ξ , from $\log \xi \sim 1.5$ to $\log \xi \sim 2.4$. There, the DEM turns over and flattens out. The consequences of the DEM shape being rather flat are explored in the next section. This DEM is sensitive to the modeled thermal stability of the plasma, as will be discussed in §7.

4.1. Volume, Scale Height, and Density Diagnostics

Consider the filling volume V of each line emission region in the optically thin limit. Note that the *DEM* is rather flat, i.e. it varies by less than an order of magnitude (once abundances are accounted for). Since $\xi \propto n_e^{-1}$, a flat DEM requires that $V \propto \xi^2$. Therefore, the region emitting Fe XXVI fills $\sim 10^2$ times more volume than the Si XIII-emitting region, and $\sim 10^4$ more volume than the N VI-emitting region. The large disparity in the volume filled by different ions can be interpreted in two ways. The first way is consistent with a model in which Fe XXVI is associated with hot corona with $\sim 10^4$ times the scale height of the compact, flattened disk atmosphere which produces N VI. A scale height ratio of the same order was calculated from the hydrostatic model atmosphere (Jimenez-Garate, Raymond, & Liedahl 2002). A second way is a scenario in which the coldest, densest part of the plasma is concentrated in small clumps, while the hottest, more diffuse part of the plasma is distributed in a large volume.

Combining plasma diagnostics, photoionization balance, and emission measure, we constrain the size and scale height of the line-emitting corona, set robust density constraints, and we estimate optical depths. For this purpose, we select Fe XXVI, Mg XI, and O VIII. For each of these ions, we plot the density n_e as a function of distance r from the X-ray source. The emitting plasma is most likely to reside inside the Roche lobe of the neutron star. The $n_e(r)$ limits drawn for Fe XXVI in Figure 9 are:

1. An upper limit on the density set by thermal and ionization balance. If the density is too high, the plasma would be too cold to emit the line, because a given line can only be emitted at a fixed range of $\xi = L/(n_e r^2)$. Thus, $n_e < L/(\xi_{\min} r^2)$, where ξ_{\min} is defined such that 95% of the line emissivity is at

$\xi > \xi_{\min}$. We take L to be the main-on luminosity, which is reprocessed into line emission during the low state.

2. A lower limit on the density given by the line flux through the emission measure EM and the maximum volume V_{\max} , such that $n_e > \sqrt{EM/V_{\max}} = \sqrt{3 EM/(4 \pi r^3)}$.

Figure 9 includes the density locus for a spherical shell of Thomson depth $\tau \sim 0.05$, which is consistent with the above limits. Such is the depth required to Compton scatter the main-on continuum and produce the continuum observed in the low state. This region of the corona extends to $\sim 10^{11}$ cm. The coronal size derived from a shallow component of an eclipse ingress is $r \gtrsim 6 \times 10^{10}$ cm: the ingress X-ray light curves exhibit a steep and fast component and a slow and shallow component, also implying a core of X-ray emission concentrated at $r \lesssim 10^9$ cm (Choi et al. 1994). High resolution spectroscopy is allowing us to probe the extended region the corona. For the Fe XXVI corona with $\tau \sim 0.05$ to be enclosed by the Roche Lobe, the scale height must be $h/r \sim 0.1$, or more conservatively, $0.01 \lesssim h/r \lesssim 0.3$.

We set stringent density constraints for the Mg XI emission region, taking advantage of the Mg XI R ratio being at its critical value (see §3.3 and Fig. 10). We calculate the same n_e limits as for Fe XXVI. In addition, we calculate the critical n_e (in the low UV flux limit), and the critical r found from UV photoexcitation (in the low density limit). These are based on the R ratio, as discussed in §3.3. This allows us to compare the derived density with the modeled density, for the case where the plasma is inside the Roche lobe. To obtain the model density at the Her X-1 main-on luminosity, we interpolate between two disk atmosphere models at L_{edd} and $0.1 L_{\text{edd}}$, and we find that the density predicted by the atmosphere model ($n_e = 3 \times 10^{13} \text{ cm}^{-3}$) is consistent with that derived directly from the R ratio. This provides support to the disk atmosphere model, because photoionization balance alone would allow one or two order of magnitude variations on n_e , depending on the optical depth of the plasma. The agreement in n_e also implies that density rather than photoexcitation effects are driving the R ratio in Mg XI.

The O VIII diagnostics in Figure 11 allow us to assign an optical depth to a given geometry. This figure shows the two n_e limits discussed previously. In addition, we plot the density of the plasma for two simple geometries: a spherical shell and a flat pill-box or atmosphere. We show two solutions with optical depths that are consistent with the density limits. The case of the spherical shell requires larger edge depths (of $\tau_{\text{O VIII}} \sim 3$) than the case corresponding to a flat atmosphere, for which $\tau_{\text{O VIII}} \sim 0.01$ in the face-on direction, as would be the case for a warped disk. The values that we will obtain from the optical depth diagnostics in §5 will favor the scenario of a flat atmosphere.

4.2. Abundances from the (N VI + N VII)/(O VII + O VIII) line ratio

Using the photoionized XSTAR and HULLAC models discussed in the beginning of §4, we quantify the relationship between the $P \equiv (\text{N VI} + \text{N VII})/(\text{O VII} + \text{O VIII})$ line *photon flux* ratio and the N/O elemental abundance ratio. Using the P ratio as an abundance diagnostic has the virtue of being independent of the EM and DEM analyses, relying instead on the XSTAR plasma models and the recombination rates obtained from the HULLAC atomic code. The XSTAR models are calculated over a grid of $\log_{10} \xi$ values that cover the range where the lines of interest are produced. We assume that the line emission is dominated by the radiative recombination process, as is shown to be the case for Her X-1 in §5. Figure 12 shows the calculated $E \equiv [\epsilon(\text{N VI}) + \epsilon(\text{N VII})] / [\epsilon(\text{O VII}) + \epsilon(\text{O VIII})]$ line *emissivity* ratio as a function of ξ , not accounting for elemental abundances (ϵ was defined earlier in §4). Therefore, we have $P = E (N/O)$, where (N/O) is the fractional abundance ratio between nitrogen and oxygen. The E and P ratios do not

depend on density. At practically any ξ at which the lines of interest are produced, $0.7 < E < 2.4$. The latter values represent the worst case error for one assuming $P \sim (N/O)$. The measured line ratio ranges from $P = 0.87 \pm 0.11$ (Jimenez-Garate et al. 2002) to $P = 1.54 \pm 0.42$ (this work). Combining these numbers, we obtain $(N/O)/(N/O)_\odot = 5.9 \pm 0.6$, using the Allende Prieto et al. (2002) and Grevesse & Sauval (1998) Solar abundances as reference, and $(N/O)/(N/O)_\odot = 9.2 \pm 1.0$ using the Wilms et al. (2000) Solar abundances. The error bars on these abundance ratios only include statistical errors. Compare this to the $4 \lesssim (N/O)/(N/O)_\odot \lesssim 8$ that can be estimated by enforcing continuity on the DEM in Figure 8.

5. Quantifying optical depth

X-ray spectroscopic analysis allows us to measure or set limits on the mean number of scatters of line photons, or to the line optical depth. The photoelectric optical depth can also be constrained by the spectrum, despite the absence of absorption edges. These measurements can have important implications for the geometry of the plasma. They also allow us to validate the previously determined elemental abundance ratios.

5.1. The mean number of scatterings for Ly α and Ly β photons

The mean number of scatterings is constrained by the observed Ly α /Ly β ratio. The Ly α /Ly β ratio is a temperature diagnostic in collisional plasmas. In contrast, this ratio depends very weakly on temperature for a recombining plasma, as we have verified from the HULLAC recombination rates. A Ly β photon from a H-like ion can get resonantly absorbed by another ion of the same species (see Fig. 13). There is a probability $\gamma = 0.12$ that the absorbed Ly β photon is converted to photons with lower energy (including an H α). Otherwise, the absorbed Ly β is re-emitted. The probability of a Ly β photon to survive N line scatterings is:

$$P = (1 - \gamma)^N = 0.88^N, \quad (7)$$

and therefore the Ly β photons cannot scatter more than a few times before getting destroyed. As the number of scatterings increases, the Ly α /Ly β intensity ratio increases with it, because Ly α photons do not get destroyed in line scatterings ($\gamma = 0$). None of the observed Ly α /Ly β line ratios shown in Table 4 show evidence for multiple line scatterings, except for O VIII. Since we deal with a large ensemble of photons, the number related to the line ratio is the mean number of scatterings $\langle N \rangle$, instead of N above.

The observed Ly α /Ly β ratio allows us to constrain the mean number of scatterings of Ly β photons directly, and of Ly α photons by inference. If $\gamma > 0$, the mean number of scatterings $\langle N \rangle$ for a slab geometry satisfies (Hummer & Kunasz 1980) :

$$\langle N \rangle = \frac{1 - \gamma}{\gamma} \frac{E_L}{E_G} \quad (8)$$

where E_L is the line energy lost to resonant absorption and E_G is the total line energy generated in the gas column. There are two relevant cases for the upper limit of $\langle N \rangle$. In the case $\gamma = 0$, photons do not get destroyed (as for Ly α), then $\langle N \rangle$ does not have an upper bound, and Equation 8 does not apply. In the case $\gamma > 0$ (as for Ly β), $\langle N \rangle$ is bounded above (by $\langle N \rangle < 7.33$), as $E_L/E_G \rightarrow 1$ in Equation 8.

We first use Equation 8 for O VIII. We detected 7 counts of the O VIII Ly β line in the 15.995 Å to 16.015 Å range. Given the continuum and background level of 3.0 counts, this represents a detection significance of 95%, as derived from a Poisson distribution. The caveat is that this is only valid if the

background is uniform in λ , and it may be subject to systematics. Since this is not a line search (i.e. the line energy is fixed), this may be a positive detection, but it needs confirmation. Taking Ly β at face value, we derive $E_L/E_G < 0.9$ for O VIII Ly β with 90% confidence, and obtain $\langle N \rangle < 6.6$. The detected line is centroided at 16.005 Å (O VIII Ly β), and it is one MEG-resolution FWHM away from Fe XVIII at 16.023 Å.

To infer the mean number of scatterings of Ly α_1 from those of Ly β , we need to relate $\langle N \rangle$ to τ , the mean line optical depth. Hummer & Kunasz (1980) performed such a calculation for a slab geometry with a uniform source of line photons, $\gamma = 0$, and Voigt parameters of 4.7×10^{-2} to 4.7×10^{-4} . They obtained $\langle N \rangle / \tau \sim 0.55\text{--}0.6$ for $\tau = 1$, of $\langle N \rangle / \tau \sim 0.60\text{--}0.65$ for $\tau = 10$, and $\langle N \rangle / \tau \sim 0.73\text{--}0.85$ for $\tau = 100$. The Voigt parameter is the ratio between the natural broadening and the velocity broadening of the line. Define $c_\tau = \langle N \rangle / \tau$. To generalize this result for $\gamma > 0$, note from Equation 2.15 in Hummer & Kunasz (1980) that $(1 - \gamma)$ can be factored out of the expression for $\langle N \rangle$, such that $\langle N \rangle = c_\tau \tau (1 - \gamma)$ is applicable in that case, with c_τ and τ as before. Note $c_\tau = c_\tau(\tau)$ is a function of τ .

The mean line optical depth τ is proportional to the oscillator strength $\tau \propto f_{\text{osc}}$. Therefore, we obtain $\langle N \rangle \propto c_\tau f_{\text{osc}} (1 - \gamma)$, from which we estimate $\langle N \rangle \sim 30$ for O VIII Ly α_1 photons. A similar number can be obtained through the more simplistic Equation 7. We ignored the continuum optical depth. The effect of a nonzero continuum depth is to decrease $\langle N \rangle$ below the derived values. Up to this point, this result depends on the detection of the Ly β line, but there is another way to deduce $\langle N \rangle$ for O VIII Ly α_1 photons.

We set an upper limit on $\langle N \rangle$ for O VIII Ly α_1 without relying on O VIII Ly β , by using the Ne X lines. This is valid since both ions are produced at a largely overlapping ionization parameter range. We find that $\langle N \rangle \lesssim 2$ for Ne X Ly β photons (at 90% confidence). Using the c_τ once again, this implies $\langle N \rangle \lesssim 9$ for Ne X Ly α_1 . The EM derived from Ne X and O VIII are the within 12% of each other, consistent with being equal given the statistical uncertainties. Scaling with the Wilms, Allen, & McCray (2000) or Allende Prieto, Lambert, & Asplund (2002) Solar abundances, we deduce $\langle N \rangle \lesssim 69$ for O VIII Ly α_1 . Scaling with CNO abundances, $\langle N \rangle$ is smaller than or equal to the latter limit. Both are consistent with the $\langle N \rangle \sim 30$ value for O VIII Ly α_1 which was derived above.

In contrast, the Ly α /Ly β ratios of Mg XII and Si XIV on Table 4 may show evidence for enhancement of Ly β due to photoexcitation effects at moderate column densities. Photoexcitation of ions by X-ray continuum photons, followed by radiative decay, can dominate the emission mechanism. This process, also referred to as resonant scattering, can produce a characteristic Ly α /Ly β ratio (Kinkhabwala et al. 2002). At low column densities, both lines are unsaturated, resonant scattering dominates over recombination emission, and the Ly α /Ly β ratio simply depends on the oscillator strengths. At moderate column density, the Ly α /Ly β ratio is reduced below the low column value, when the Ly α line reaches saturation but the Ly β line does not. The evidence for photoexcitation of Mg XII and Si XIV at the moderate column density regime is a $\sim 2\sigma$ result, so we do not discuss this scenario further. At high column densities, recombination emission dominates over resonant scattering, because resonant scattering has completely saturated while the emission measure keeps growing with the column, and the Ly α /Ly β ratio is determined by the ratio of the recombination efficiency of the lines, which happens to be similar to the oscillator strength ratio. In this section we have expanded upon the Kinkhabwala et al. (2002) picture, showing that at high line optical depths, the Ly α /Ly β ratio can increase above its pure recombination value due to the destruction of the Ly β line.

5.2. The optical depth of the r line in He-like ions

The value of the $G = (i + f)/r$ ratio depends on whether the plasma is collisionally ionized or photoionized, but it can also be used to quantify the mean optical depth of the r line. The G ratio depends on optical depth for three reasons: 1) the r line has much larger oscillator strength than either the i or f lines; 2) the recombination rates of the i, f lines are larger than those of the r line, because the i, f lines have larger statistical weight than the r line; and 3) the G ratio depends very weakly on temperature in a photoionized plasma. This diagnostic has been quantified by Kinkhabwala et al. (2002) and Wojdowski et al. (2003). In the limit of small line optical depth, we have $G \sim 0.3$, because the r line is enhanced relative to the f and i lines by continuum X-rays that photo-excite the ground state (Wojdowski et al. 2003). In the small line depth regime, the emission is dominated by resonant scattering over recombination emission. In this regime, the line spectrum is dependent on the spectral energy distribution. In the limit of large line optical depth, G reaches an asymptotic value of 4.5 (Porquet & Dubau 2000), which depends very weakly on the T values derived from photoionization equilibrium, and recombination emission dominates over resonant scattering.

The observed G ratios shown in Table 3 are consistent with the limit of large line optical depth. By using the lower bounds on G , we can set lower limits on the mean depth of the r lines as defined by Wojdowski et al. (2003), of $\tau_r \gtrsim 100$ for $G > 4$ (the maximum value applicable to Ne IX and O VII), $\tau_r \gtrsim 20$ for $G > 3$ (applicable to Mg XI), and $\tau_r \gtrsim 10$ for $G > 2$ (applicable to Si XIII), assuming a continuum power-law index of $\alpha = 1.0$. The observed main-on index is $\alpha = 0.85$, but G depends weakly on α .

5.3. An X-ray atmosphere illuminated at a small grazing angle has anisotropic line depths

If the plasma geometry is anisotropic, the line optical depth will depend on direction. A first special direction vector corresponds to the path of the X-ray continuum photons from the X-ray pulsar, since this radiation is photoionizing the plasma. The second special direction is that which minimizes the optical depth, since photons will tend to escape from the plasma that way. Based on this, we define two relevant depths: an “illumination” optical depth τ_i , and an “escape” optical depth τ_e , which are well-defined and not equal if the plasma distribution is illuminated along a direction where the optical depth is not minimized. The illumination depth τ_i determines how much of the continuum radiation is absorbed, and therefore how much is reprocessed into resonant and recombination emission lines. On the other hand, once a line photon is produced, it is more likely to escape in the direction where the optical depth is minimized than through other directions, and this corresponds to the escape depth τ_e .

The $\text{He}\alpha$ G ratio is sensitive to τ_i , because G depends on the ratio between the resonant scattering and recombination line fluxes, as mentioned in the previous section. Further scattering of the r line after it is produced does not destroy it unless the continuum depth is significant. On the other hand, the $\text{Ly}\alpha/\text{Ly}\beta$ ratio is sensitive to both τ_i and the escape depth τ_e . Again, resonant line absorption of $\text{Ly}\alpha$ or $\text{Ly}\beta$ produces a dependency on τ_i , because both photons resonant scatter strongly. In addition, the $\text{Ly}\beta$ photon can be destroyed and converted to $\text{Ly}\alpha$ if it scatters too many times inside the plasma, and this is why the dependence on the escape depth τ_e arises.

The flat, geometrically thin shape of the model disk atmosphere is anisotropic, and the atmosphere is illuminated by the neutron star at a very shallow grazing angle that was determined from self-consistent calculations (Jimenez-Garate, Raymond, & Liedahl 2002). This geometry is shown schematically in Figure 14. In the atmosphere model, the calculated grazing angle is such that illumination depth is 25 times

larger than the escape depth at $r = 10^{11}$ cm, and therefore the observed $\text{He}\alpha$ r line depth is expected to be much larger than the $\text{Ly}\beta$ depth. Sample vertical column densities in the disk atmosphere model are $N_{\text{OVIII}} = 5 \times 10^{17} \text{ cm}^{-2}$, $N_{\text{OVII}} = 2 \times 10^{17} \text{ cm}^{-2}$, and $N_{\text{SiXIII}} = 1.6 \times 10^{16} \text{ cm}^{-2}$. These columns imply escape line depths of $\tau_e \sim 46$ ($150 \text{ km s}^{-1}/v$) for O VIII $\text{Ly}\alpha_1$, $\tau_e \sim 53$ ($150 \text{ km s}^{-1}/v$) for O VII r , and of $\tau_e \sim 1.4$ ($150 \text{ km s}^{-1}/v$) for Si XIII r , where v a fiducial velocity width that includes thermal and turbulent components. Setting v to the thermal value at $kT = 25 \text{ eV}$ for O VIII yields $\tau_e = 178$ for $\text{Ly}\alpha_1$, and setting $kT = 3.5 \text{ eV}$ for O VII yields $\tau_e = 544$ for $\text{He } r$. Note that $\tau_i \sim 25\tau_e$ for the disk model geometry, i.e. for Si XIII we get $\tau_i = 36$ ($150 \text{ km s}^{-1}/v$). These are the expected line depths from the disk atmosphere model, modulo the assumptions made about the gas kinematics.

Compare the above values with the optical depth measurements from $\text{Ly}\alpha/\text{Ly}\beta$ that yielded $\langle N \rangle \sim 30$ for O VIII $\text{Ly}\alpha_1$, which is equivalent to $\tau \sim 46$ given the calculated $\langle N \rangle/\tau$ ratios and Voigt parameters from §5.1. This optical depth matches the model at the chosen 150 km s^{-1} velocity width. If the O VIII $\text{Ly}\beta$ line detection is not real, from Ne X it follows that for O VIII $\text{Ly}\alpha_1$ still $\tau \lesssim 100$. This would simply require a smaller velocity width than above, so there is parameter space available to achieve consistency of the data with the disk atmosphere model in this case. For the case of O VII, an upper limit $\tau_r > 100$ was obtained from the G ratio, which is easily accommodated by $\tau_i \sim 1300$ ($150 \text{ km s}^{-1}/v$) for the illumination depth. This large τ_i leaves plenty of parameter space to be consistent with the other lower limits on τ_r set for Ne IX, Mg XI, and Si XIII. For example, Si XIII was measured to have $\tau_r \gtrsim 10$, which is consistent with the atmosphere model $\tau_i = 36$. For reference, the model escape depth for the continuum is $\tau_e(\text{OVIII}) = 0.05$, an illumination depth $\tau_i(\text{OVIII}) = 1.2$.

Our results above depend on the estimated kinematics, and therefore are only approximate consistency checks. Since the velocity field in the disk is produced by both Keplerian and turbulent motions, τ_e will in fact be highly anisotropic, and it will depend on the photon momentum vector relative to the disk velocity field. To self-consistently derive a turbulent velocity from the $\text{Ly}\alpha/\text{Ly}\beta$ ratio, one requires a calculation of the line transfer which accounts for this velocity field.

5.4. RRC/RR ratios and electron temperature

The electron temperature measured from the Ne IX RRC is $kT = 7 \pm 3 \text{ eV}$, or $T = 81000 \pm 35000 \text{ K}$. This was measured by fitting the semi-Maxwellian profile of the Ne IX RRC at $\lambda = 10.37 \text{ \AA}$, the brightest RRC in the spectrum, detected at the 5σ level (see Fig. 3). The XSTAR plasma code and the HULLAC recombination rates yield emissivity-weighted average temperatures kT_o which are shown on Tables 4 and 5. The T_o for Ne IX is in good agreement with the measured T . The significance of detection for other RRCs obtained with the Cash statistic ranges from the 2σ to the 5σ level (see Table 1). To fit the RRCs, we rebin the spectra to bin sizes $\Delta\lambda$ of 0.05 \AA to 0.09 \AA (coarser than the bin size used for fitting lines). While most RRCs do not have sufficient statistics for an accurate T measurement, T is left as a free parameter and the best-fit values are consistent with T_o for most cases.

In Table 5, we show the observed RRC to RR (radiative recombination lines) flux ratios, compared to the HULLAC calculations, in the recombination-dominated case, for both a single temperature model and for the disk atmosphere model. The RRC/RR ratios for O VII, O VIII, and Ne X are significantly weaker than expected for the single- T model, but agreement is generally better for the disk atmosphere model, which accounts for a broad distribution of temperatures $2 < kT < 860 \text{ eV}$. It is therefore likely that the RRCs are composed of multiple temperatures, with the low- T component being observed more readily than the high- T

component. The high- T RRC component, which usually dominates the recombination flux, is too broad to be separable from the continuum. In this favored scenario, the weak RRCs are simply an indication of the multi- T nature of the plasma.

5.5. Verification of CNO abundances: the line optical depths are not large enough to convert O VIII Ly α to N VII Ly α

We test for the presence of the X-ray Bowen fluorescence mechanism by which a O VIII Ly α line becomes a N VII Ly α line, as calculated by Sako (2003). We determine whether this X-ray Bowen fluorescence effect can account self-consistently for the apparent excess intensity observed in N VII Ly α , N VI i and r , and the N VII RRC with respect to other lines, such as the O VIII Ly α and O VII i and r . We find that:

1. The X-ray Bowen fluorescence mechanism is unlikely to enhance N VI He α emission in the same proportion as N VII Ly α . This would require line opacities to overlap in energy space under nearly identical conditions as those found for N VII Ly ζ and O VIII Ly α_2 , whose energies are 1 Doppler width away at $T = 50$ eV. We checked for coincidences between the energies of the brightest lines of abundant elements in the 22.46 to 26 Å band and the resonance line energies of N VI. We did not find line overlaps closer than 46 Doppler widths at $T = 50$ eV, and the number of Doppler widths is likely to be higher since models show a peak N VI He α flux at $T = 2.8$ eV. As shown in the HETGS spectrum in Fig. 4, as well as from the *XMM-Newton* RGS spectrum (Jimenez-Garate et al. 2002), both N VI He α and N VII Ly α indicate a N over-abundance.
2. The measured mean number of scatterings of O VIII Ly α and Ly β photons is two orders of magnitude lower than required for the X-ray Bowen fluorescence effect to take place. The measured line ratio between O VIII Ly α and Ly β depends on $\langle N \rangle$, due to the destruction of Ly β or its conversion to Ly α . We derive $\langle N \rangle \sim 30$ for O VIII Ly α_1 . This was verified via the same ratio in Ne X, which scales to $\langle N \rangle \lesssim 69$ for O VIII Ly α_1 with Solar or CNO abundances (see §5.1). Compare this to the $\langle N \rangle \sim 5 \times 10^3$ scatterings needed for the N VII enhancement (Sako 2003).
3. The detection of the N VII RRC with *XMM-Newton* and *Chandra* provides additional evidence for a N/O overabundance. At the escape line depths implied by the measured Ly α /Ly β ratios, the RRC fluxes are unaffected by optical depth effects. The N VII RRC detected with *XMM-Newton* RGS (Jimenez-Garate et al. 2002) at 10σ has flux $(6.5 \pm 2.8) \times 10^{-5}$ ph cm $^{-2}$ s $^{-1}$, with 90% confidence errors, and HETGS detected it at 3.5σ with flux $(18 \pm 5) \times 10^{-5}$ ph cm $^{-2}$ s $^{-1}$, with 68% confidence errors (Table 1). These fluxes are larger than the $\lesssim 1 \times 10^{-5}$ ph cm $^{-2}$ s $^{-1}$ expected from Solar abundances and the fluxes of O VII RRC and O VIII RRC.
4. An analysis of the UV line emission from Her X-1 using the same sort of illuminated disk model concluded that N was over-abundant in HZ Her, with a N/C abundance ratio of ~ 2 (Raymond 1993), which implies a N overabundance relative to Solar of ~ 6 . This shows that both UV and X-ray disk emission models yield consistent results.
5. The velocity shear in the disk atmosphere and corona increases the line escape probability, which would decrease $\langle N \rangle$ below the static values calculated by Sako (2003) for a given column density. This suppresses X-ray Bowen Fluorescence.

We conclude that the large nitrogen over-abundance interpretation of the Her X-1 spectrum by Jimenez-Garate et al. (2002) is valid and cannot be self-consistently explained by the X-ray Bowen fluorescence effect. The large nitrogen over-abundance implies that significant CNO processing occurred in a massive star in the system. New transfer calculations are required to improve the optical depth and dynamical constraints on the accretion flow. Such calculations need to include thermal and ionization balance, stratification, and gas orbital kinematics in order to calculate line transfer more accurately than existing models.

6. Comparison with an accretion disk atmosphere and corona model

In Figs. 2–4 we over-plot the synthetic spectrum of an illuminated accretion disk atmosphere and corona model from Jimenez-Garate, Raymond, & Liedahl (2002). We compare the data to this disk atmosphere model. The model assumes that the neutron star continuum energizes the vertically stratified structure of a hydrostatic accretion disk in thermal and ionization balance. We used two adjustable parameters to fit the spectrum: a normalization factor of $N = 0.11$, and the disk radius range $10^{10.9} < r < 10^{11}$ cm (the outer annulus in the model). Both parameters affect the normalization and do not influence the spectral shape. We did not include any Doppler velocity broadening effects. The ionizing continuum in the model consists of a bremsstrahlung with $T = 8$ keV and a luminosity $L_x = 10^{38.3} (D/6.6 \text{ kpc})^2 N \text{ erg s}^{-1}$. Given the approximate linear dependence of line flux on continuum flux (Jimenez-Garate, Raymond, & Liedahl 2002), the effective ionizing luminosity in the model fit was $L_x = 2.3 \times 10^{37} \text{ erg s}^{-1}$. This is nearly the unabsorbed luminosity during main-on state of Her X-1 in the 0.1–200 keV band, $L = 3.8 \times 10^{37} \text{ erg s}^{-1}$ (dal Fiume et al. 1998). The model normalization can be interpreted as simply a geometrical parameter which indicates that the observed emission is produced by an outer section in the accretion disk atmosphere and corona with area $A \sim 3 \times 10^{21} \text{ cm}^2$. That A is a small fraction of the total disk area is in agreement with observing an outer disk rim, as suggested by the small velocity broadening of the emission lines (§3.2). The neutron star continuum observed during the main-on powers the recombination emission observed during the low state. The precession of the accretion disk allows us to isolate the reprocessed emission from the direct emission from the neutron star.

The relative strengths of the spectral lines, which are fixed in the model, are a direct measure of the structure of the accretion disk atmosphere and corona. In general, they constrain the temperature, ionization, and density distributions. In the context of our model, the relative line strengths are indicators of the vertical ionization structure of the disk atmosphere and corona, since the ionization level and temperature are stratified with vertical depth. In Table 1, we compare the relative strengths of lines with different ionization parameters (except for Fe K α fluorescence at 1.94 Å, which is fit separately, because it is not yet calculated in the disk model). We note that the relative strengths of the Ly α lines of S XVI, Si XIV, Mg XII, Ne X, and O VIII lines were fit with $\sim 50\%$ or better accuracy, with *virtually zero degrees of freedom*, because N and the radius range, the two free parameters in the model, only affect the overall flux normalization. Since O VIII and S XVI are produced at ionization parameters that are one order of magnitude apart, it is a notable success for the model to be able to reproduce their flux ratios. In the disk model context, this indicates that the emission measure distribution of the upper half of the atmosphere agrees well with the data. The incidence angle on the disk atmosphere is self-consistently determined by the model (Jimenez-Garate, Raymond, & Liedahl 2002).

The Fe XXVI Ly α line probes the hottest and most extended region of the disk corona observed with HETGS (see §4.1 and Fig. 2). The XSTAR photoionization equilibrium plasma model (Kallman & McCray 1982), coupled with the recombination rates obtained with the HULLAC atomic code (Klapisch et al. 1977),

show that the electron temperature of the plasma producing the Fe XXVI line is $T_e \sim 6.7 \times 10^6$ K, with ionization parameter $\log \xi \sim 3.8$. Similar parameters are obtained with the disk atmosphere model. The observed Fe XXVI Ly α line flux is 3.9 times larger than the disk model's. Judging from the disk model, the Fe XXVI H α and H β recombination lines at 9.68 Å and 9.53 Å (see Fig. 3 and Table 1) are 10 times weaker than expected. The flux ratio of H α and Ly α lines is not expected to depend strongly on temperature in the pure photoionization case. The Fe XXVI Ly α line was also detected with *XMM-Newton* (Zane et al. 2004). An emission line of Fe XXV at 1.85 Å appears in the model, as well as a Fe XXIV complex with lines at 11.18 Å, 11.03 Å, and 10.62 Å (these lines appear in Fig. 3). None of these relatively weak lines are detected. In short, the upper coronal structure appears to be more ionized and to have a larger emission measure in Her X-1 than in the disk atmosphere and corona model.

We have shown that several key characteristics of the X-ray recombination spectrum can be explained by an outer section of the accretion disk which is being illuminated by the neutron star. This disk atmosphere model describes much of the Her X-1 X-ray line spectrum from first principles. However, there are discrepancies between the model and the data. One notable discrepancy is N VII and N VI, which are under-predicted by a factor of ~ 10 . This is consistent with the §4.2 results. Also, the He-like ion line fluxes are systematically underpredicted by the model, as we discuss below.

7. Thermal stability of the photoionized plasma and the H-like/He-like ion line ratios

A thermal instability has been predicted to be present in plasmas which are photoionized by an X-ray continuum. The “type I” instability is produced by an imbalance between bremsstrahlung cooling and Compton heating, just below the Compton temperature (Krolik, McKee, & Tarter 1981). The “type II” instability is produced by the imbalance between recombination cooling and photoionization heating (Kallman 1984). The photoionized disk atmosphere models predict a type II instability regime at $6 \times 10^4 < T < 5 \times 10^5$ K (Jimenez-Garate, Raymond, & Liedahl 2002). X-ray recombination emission is suppressed in the latter regime. The recombination line fluxes are sensitive to the ion fraction $f_{i+1}(\xi)$. The instability reduces the interval $[\log \xi_o - \Delta(\log \xi), \log \xi_o + \Delta(\log \xi)]$ at which $f_{i+1} \gtrsim 0.1$. For this reason, the disk atmosphere model predicts very weak Mg XI line fluxes relative to Mg XII, contrary to observations (as shown in Fig. 3). The DEM analysis indicates that the Mg XI flux is above the expectation (Fig. 8). The ions with ξ_o near the instability regime will have their line power reduced and their derived DEM increased.

The He-like ion lines of Si XIII, Mg XI, Ne IX, O VII, and N VI are underpredicted by the atmosphere model. Also, the DEMs derived from the same He-like ions are systematically larger than the DEMs from the H-like ions. This may imply that the plasma is more thermally stable than the models predict, or it may require a larger EM of $T \sim 10^5$ K plasma. The He-like ion lines are especially sensitive to the thermal instability because of a key physical difference: the H-like ions form by the recombination of fully stripped atoms, so their line emissivities are less sensitive to ξ than those of He-like ions. The $f_{i+1}(\xi)$ for the He-like lines are single-peaked functions, while the $f_{i+1}(\xi)$ for the H-like lines are asymptotic curves with $f_{i+1} \rightarrow 1$ as $\xi \rightarrow \infty$, and $f_{i+1} \rightarrow 0$ as $\xi \rightarrow 0$. This causes the line emissivities for the He-like ions to have narrow peaks and small $\Delta(\log \xi)$, while in contrast, the line emissivities of H-like ions have broad asymmetric peaks with large $\Delta(\log \xi)$, with tails that extend to large ξ . This is why, in spite of a possible overlap of the ξ of formation between the He-like and H-like ions, the H-like ion line fluxes will still dominate over the He-like ion lines at high ξ . Therefore we expect the He-like ion lines to be more sensitive indicators of the ionization distribution and the instability regime than the H-like ion lines. The changing trends of the EM in Figure 7 compared to the DEM in Figure 8, suggest that the thermal instability regime is larger in the models than

in the plasma, but this is difficult to ascertain without a systematic study of the plasma models.

The n_e measurement from Mg XI He α (§4.1) also tests stability of the photoionized plasma, since the disk atmosphere model predicts a regime of forbidden density. The n_e regions allowed by both the spectral diagnostics and disk atmosphere models are shown in Figure 10. The density of formation for Mg XI is $n_e = 3 \times 10^{13} \text{ cm}^{-3}$ according to the disk atmosphere model. The forbidden densities are just below that, at $2 \times 10^{12} < n_e < 3 \times 10^{13} \text{ cm}^{-3}$. The measured $n_e = (2 \pm 1) \times 10^{13} \text{ cm}^{-3}$ is located in the high density end of the stable regime. The thermal instability calculation in the disk model is in agreement with the observations in this case.

The X-ray spectroscopic data is now sufficiently detailed that it is possible to start testing the regimes of thermal instability in the photoionized plasma. On the one hand, a DEM analysis based on XSTAR plasma models and the HULLAC recombination rates suggests that the plasma is more thermally stable than was originally predicted. On the other hand, the density constraints from the R ratio of Si XIII indicate that the density is just at the edge of the stability region, as derived from the disk atmosphere model. Further, the same disk atmosphere model predicts the Mg XI He α flux to be suppressed due to the instability, but no such suppression is observed.

8. X-ray Spectral Comparison with other LMXBs

We compare the spectral properties of the Her X-1 low state with two low-mass X-ray binaries: 4U 1822-37 and 2S 0921-63. Both 4U 1822-37 and 2S 0921-63 are classified as ADC sources. These LMXBs exhibit X-ray emission lines with unresolved velocity broadening. The limits on the velocity widths (FWHM) of the recombination lines measured with Chandra HETGS are $\Delta v < 1500 \text{ km s}^{-1}$ for 2S 0921-63 (Kallman, Angelini, Boroson, & Cottam 2003), $\Delta v < 300 \text{ km s}^{-1}$ for 4U 1822-37 (Cottam et al. 2001), and $\Delta v < 260 \text{ km s}^{-1}$ for Her X-1 (from O VII in Table 1). Her X-1 and 4U 1822-37 exhibit RRCs that indicate that photoionization is the dominant ionizing mechanism in the plasma. In 2S 0921-63, the bright O VII intercombination line (giving the value of $G \sim 4$ for that diagnostic line ratio) is indicative of a photoionized plasma (Kallman, Angelini, Boroson, & Cottam 2003). The non-detection of RRCs in 2S 0921-63 is likely due to the low signal-to-noise ratio of the emission features. The weak or undetected Fe L-shell lines in these LMXB spectra are yet another signature of photoionization. It is therefore clear that the lines in these LMXBs are produced by recombination following photoionization.

When looked at more carefully, a comparison of the spectra of 4U 1822-37, 2S 0921-63, and Her X-1 reveals a nuanced picture. First, the continuum level varies significantly from source to source: 4U 1822-37 has ~ 10 times larger continuum flux in the 0.5–7 keV band than 2S 0921-63 or Her X-1. The continuum in 4U 1822-37 is harder than in the other two sources. Second, the soft X-ray line spectra in 4U 1822-37 and Her X-1 appear to be quite similar, i.e. the fluxes of the Si XIV, Mg XII, Mg XI, Ne X, Ne IX, O VIII, and O VII lines are roughly within tens of percent of each other, albeit the exact line ratios and density diagnostics differ. On the other hand, 2S 0921-63 shows weaker line fluxes than 4U 1822-37 and Her X-1, perhaps because the eclipse is blocking the source of the line emission. Third, the line ratios between Fe emission lines from both high and low ionization species are different. Her X-1 exhibits a much more intense Fe K α line from Fe I–Fe XIII at 1.94 Å than 2S 0921-63, but a nearly equal flux of the Fe XXVI line at 1.78 Å. 2S 0921-63 exhibits both Fe XXV and Fe XXVI lines with nearly equal fluxes, and a Fe K α fluorescence line with 1/4 of the flux of the Fe XXV/Fe XXVI lines (Kallman, Angelini, Boroson, & Cottam 2003). It is conceivable that the fluorescing material was occulted by the eclipse of 2S 0921-63, while the hotter, more

extended emission was not. 4U 1822-37 also showed Fe K α and Fe XXVI lines, with Fe K α being brighter (Cottam et al. 2001), but it did not show the large flux contrast between those lines observed in Her X-1. Fourth, the N VII Ly α and N VI He α lines are most intense in Her X-1 (see Fig. 4). So far, other LMXBs and ADC have not shown such strong N lines, albeit the measurement is rendered difficult for most cases due to the large absorbing hydrogen columns N_{H} that are common in these systems. In §4 and §5.5, we quantified this abundance anomaly, which was also observed with the *XMM-Newton* RGS (Jimenez-Garate et al. 2002).

We now compare X-ray flux variability with orbital phase. While our observations of Her X-1 are restricted to mid-orbit at $0.33 < \phi < 0.67$, the 2S 0921-63 observations were restricted to mid-eclipse, and the 4U 1822-37 observations spanned full orbits. The emission during the 2S 0921-63 eclipse originates in either the outer disk rim or in an extended circumsource region (such as a corona) with an upper size limit of 7×10^{10} cm (Kallman, Angelini, Boroson, & Cottam 2003). The emission line region in 4U 1822-37 was identified to be the illuminated disk bulge, because the line fluxes were observed to peak at $\phi \sim 0.25$ (Cottam et al. 2001). Flux variations were not observed in Her X-1, but with the limited phase coverage we can ascertain that it does not show the same sort of variation than 4U 1822-37. Judging from the spectral variations as a function of orbital phase, the azimuthal location of the line emission regions in Her X-1, 2S 0921-63, and 4U 1822-37 appears to be distinct amongst these sources.

Her X-1, 4U 1822-37 and 2S 0921-63 are sources that are observed at high-inclination angles ($85^\circ \lesssim i < 90^\circ$), which causes the accretion disk to block the direct X-ray emission from the accreting object. ADCs have a higher optical-to-X-ray flux ratio than other LMXBs, which is a well-known indicator that the accreting object is not observed directly (White, Nagase, & Parmar 1995, and references therein). This, in turn, causes the EWs of the X-ray emission lines in ADCs to be much larger than in other LMXBs, because only $\sim 10^{-2}$ – 10^{-3} of the available continuum energy is reprocessed into recombination lines. This scenario is consistent with the model presented in §6, where only a fraction of the accretion disk area can account for the line emission. Incidentally, the only other ADC for which a high-resolution spectrum was obtained is AC 211 (in the M15 cluster), but it did not show emission lines (White & Angelini 2001), probably due to contamination from a bright and nearby LMXB burster.

In sum, high-inclination LMXBs exhibit recombination-dominated line spectra and unresolved line broadening. The illuminated disk bulge seen in 4U 1822-37, however, is not observed in Her X-1 with the current data, and only the extended emission during eclipse was observed in 2S 0921-63. A definitive comparison of the accretion flow geometry of these sources will require new spectral data with good orbital phase coverage for Her X-1 and 2S 0921-63.

9. Conclusions

1. We detect more than two dozen spectral features in the X-ray spectrum of the Hercules X-1 low state with the *Chandra* HETGS. Most of the observed features correspond to the recombination signatures expected from a centrally illuminated accretion disk atmosphere and corona located in the outer accretion disk, given the following evidence:

- Using photoexcitation diagnostics with the He-like ion lines, coupled with the observed ultraviolet continuum fluxes by Boroson et al. (2001), we ruled out the possibility that the *recombination* emission lines originate on the illuminated companion star, HZ Her.
- The spectral model for a centrally illuminated accretion disk atmosphere and corona fit most of

the observed fluxes and ratios of the X-ray recombination lines. The model requires the low state emission to be energized by the continuum observed in the high state. The caveat is that the He-like lines are underpredicted by the model, and the observed line broadening is smaller than expected for a plasma corotating with the accretion disk. The small Doppler widths may be due to vignetting effects that allow only the far edge of the disk to be visible, as would occur for an edge-on disk with a flared or warped geometry. In support of this, the model fits indicate that only the outer rim of the disk ($8 \times 10^{10} < r < 10^{11}$ cm) is observed, in contrast with LMXBs such as EXO 0748-67, where much of the inner disk emits observable X-ray lines (Jimenez-Garate, Schulz, & Marshall 2003).

- The measured R line ratio of Mg XI allows us to precisely determine a density of $n_e = (2 \pm 1) \times 10^{13}$ cm $^{-3}$, which agrees with the disk atmosphere model predictions ($n_e = 3 \times 10^{13}$ cm $^{-3}$). This corresponds to the low UV field limit, which is the most likely scenario for Mg XI. Using UV observations (Boroson et al. 2001), we deduce that the disk may be far enough from HZ Her for the Mg XI triplet to be unaffected by photoexcitation. The presence of UV emission and high- n_e necessitates the re-calculation of R ratios in (n_e, F_{UV}) space.
- The X-ray spectrum probes radically different length scales in the atmosphere and corona. For example, an emission measure analysis shows that the volume where Fe XXVI is emitted must be $\sim 10^4$ times larger than that for N VI. Compare this to the cool model atmosphere emitting N VII at $T \sim 32500$ K, with 10^7 cm thickness, and 3×10^{13} cm $^{-3}$ density, which coexists with a 10^{10} cm thick hot corona emitting Fe XXVI, with 10^{11} – 10^{12} cm $^{-3}$ density and $T \sim 10^6$ K (with intermediate layers of ionization in between).
- The RRC/RR ratios and the measured $T = 81000 \pm 35000$ K from Ne IX RRC are generally in agreement with the disk atmosphere model. Single- T models do not reproduce well the observed RRC/RR flux ratios of H-like ions, while the disk model produces improved agreement. This indicates the presence of multiple temperature components, since any high- T component of the RRCs is lost in the continuum.
- The line depths derived from the spectrum via the Ly α /Ly β and G ratios are consistent with the ionic column densities and flattened geometry of the model disk atmosphere, where the first ratio is most sensitive to escape depth (vertical depth) and the second is determined by the grazing incidence depth. To obtain consistency, we use a turbulent velocity width of $\Delta v \sim 150$ km s $^{-1}$. We rely on the relationship between τ and the mean number of scatters $\langle N \rangle$ calculated for a range of Voigt parameters by Hummer & Kunasz (1980).

2. We find a prominent Fe K $\alpha_1, \alpha_2, \beta$ complex indicative of a neutral plasma. We cannot ascertain whether the Fe K fluorescence is produced in the disk or on HZ Her, or both. The Fe K α line flux from HETGS does not vary with orbital phase at $0.3 \lesssim \phi \lesssim 0.7$, but Zane et al. (2004) did observe a clear modulation with ϕ with *XMM-Newton*.
3. The lines in the X-ray spectrum have unresolved velocity broadening ($\Delta v < 260$ km s $^{-1}$), similar to what has been observed for the lines in ADC sources. This is evidence that the accretion disk is edge-on with respect to our line of sight. Previously observed spectral changes with the *XMM-Newton* RGS showed a transition between broad lines in the main-on state and narrow lines in the short-on and low states, which suggested emission from the inner disk during main-on and from the outer disk during short-on and low state (Jimenez-Garate et al. 2002). The well-known 35 d flux modulation has long been attributed to the precession of an edge-on disk.

4. By measuring the mean number of line scatterings, we rule out the presence of the X-ray Bowen fluorescence effect calculated by Sako (2003). We constrain the mean number of scatterings of the O VIII Ly α_1 line to $\langle N \rangle \lesssim 69$. The upper limit is based on the detection of O VIII and Ne X Ly β lines, which must be destroyed after a large number of scatterings. In contrast, the X-ray Bowen fluorescence effect would require $\langle N \rangle \sim 5 \times 10^3$. Therefore, the N VII/O VIII Ly α line ratio is unaffected by optical depth effects.
5. The signature of CNO abundances observed with *XMM-Newton* (Jimenez-Garate et al. 2002) is confirmed. Strong N VI He α , N VII Ly α , and N VII RRC lines are present in the HETGS and in the *XMM-Newton* RGS spectra. The N abundance is verified to be higher than Solar. The simplest EM analysis, the DEM analysis, and the $(N\text{ VII} + N\text{ VI})/(O\text{ VII} + O\text{ VIII})$ line ratio yield $4 \lesssim (N/O)/(N/O)_\odot \lesssim 9$. The uncertainty is dominated by systematics in the analysis rather than by the effective area calibration. The depletion of carbon derived from the RGS data is also evidenced in our DEM analysis. This is supported by measurements of the N/C ratio made by comparing the observed UV spectrum to that from an illuminated accretion disk model (Raymond 1993). The relative O abundance is sensitive to the Solar abundance values, being under-abundant with the Wilms, Allen, & McCray (2000) values, and consistent with Solar with the Allende Prieto, Lambert, & Asplund (2002) values.
6. Given the problems with fitting the He-like ion line fluxes with either the disk model or the DEM, we deem that either a) the thermal instability regime is over-predicted; or 2) the disk atmosphere model requires more emission measure at $T \sim 10^4\text{-}10^5$ K. The He-like ion lines are more sensitive probes of the thermal equilibrium of the plasma than the H-like ion lines. It is possible that the thermal instability has been over-estimated in the models, therefore cutting the He-like ion fluxes disproportionately. However, the density diagnostics seem to be consistent with the calculated stable density values.
7. There are line transfer effects which remain to be accounted for in the models, such as the competition between line emission by photoexcitation and line destruction, and the effects of repeated photoionizations and recombinations produced by lines and RRC. However, the Her X-1 spectrum indicates that these are second-order effects, compared to the pure recombination emission.
8. The atmospheric and coronal components unveiled by the X-ray line spectra are more extended ($10^{10} - 10^{11}$ cm), cooler, less luminous, and have smaller vertical Thomson depth ($\tau_T \sim 0.01$) than the compact (10^9 cm) ADC component with $\tau_T \gtrsim 1$, which resides close to the compact object. Indeed, *both* compact and extended ADC components are evident in the eclipse ingress light curves observed in Hercules X-1 (Choi et al. 1994). Therefore the plasma observed in high resolution spectra is not part of what is commonly referred to as an ADC (i.e. a fully ionized spherical distribution of plasma that is Thomson scattering the neutron star X-rays), but instead may be a continuation of it at the Roche lobe scale. The extended ADC component observed in eclipse coincides with our size measurements for the X-ray line region.

REFERENCES

Allende Prieto, C., Lambert, D. L., & Asplund, M. 2002, ApJ, 573, L137

Bautista, M. A. & Kallman, T. R. 2000, ApJ, 544, 581

Boroson, B., Vrtilek, S. D., McCray, R., Kallman, T., & Nagase, F. 1996, ApJ, 473, 1079

Boroson, B., Blair, W. P., Davidsen, A. F., Vrtilek, S. D., Raymond, J., Long, K. S., & McCray, R. 1997, *ApJ*, 491, 903

Boroson, B., Kallman, T., Vrtilek, S. D., Raymond, J., Still, M., Bautista, M., & Quaintrell, H. 2000, *ApJ*, 529, 414

Boroson, B., Vrtilek, S. D., Kallman, T. R., Still, M., Quaintrell, H., McCray, R., Greene, J., & Raymond, J. 2001, *Bulletin of the American Astronomical Society*, 33, 1446

Canizares, C. R. et al. 2000, *ApJ*, 539, L41

Cann, N. M., & Thakkar, A. J. 1992, *Phys. Rev. A*, 46, 9, 5397

Chiang, J. 2001, *ApJ*, 549, 537

Choi, C. S., Dotani, T., Nagase, F., Makino, F., Deeter, J. E., & Min, K. W. 1994, *ApJ*, 427, 400

Clayton, D. D. 1983, *Principles of Stellar Evolution and Nucleosynthesis* (Chicago: University of Chicago Press)

Cottam, J., Sako, M., Kahn, S. M., Paerels, F., & Liedahl, D. A. 2001, *ApJL*, 557, L101

dal Fiume, D. et al. 1998, *A&A*, 329, L41

Deeter, J. E., Boynton, P. E., Miyamoto, S., Kitamoto, S., Nagase, F., & Kawai, N. 1991, *ApJ*, 383, 324

Gerend, D. & Boynton, P. E. 1976, *ApJ*, 209, 562

Giacconi, R., Gursky, H., Kellogg, E., Levinson, R., Schreier, E., & Tananbaum, H. 1973, *ApJ*, 184, 227

Grevesse, N. & Sauval, A. J. 1998, *Space Science Reviews*, 85, 161

Houck, J. C. & Denicola, L. A. 2000, in *ASP Conf. Ser. 216, Astronomical Data Analysis Software and Systems IX*, ed. N. Manset, C. Veillet, & D. Crabtree (San Francisco: ASP), 591

Hummer, D. G. & Kunasz, P. B. 1980, *ApJ*, 236, 609

Jimenez-Garate, M. A., Schulz, N. S., & Marshall, H. L. 2003, *ApJ*, 590, 432

Jimenez-Garate, M. A., Raymond, J. C., & Liedahl, D. A. 2002, *ApJ*, 581, 1297

Jimenez-Garate, M. A., Hailey, C. J., Herder, J. W. d., Zane, S., & Ramsay, G. 2002, *ApJ*, 578, 391

Kahn, S. M., Leutenegger, M. A., Cottam, J., Rauw, G., Vreux, J.-M., den Boggende, A. J. F., Mewe, R., & Güdel, M. 2001, *A&A*, 365, L312

Kallman, T. R., Angelini, L., Boroson, B., & Cottam, J. 2003, *ApJ*, 583, 861

Kallman, T. R. & McCray, R. 1982, *ApJS*, 50, 263

Kallman, T. R. 1984, *ApJ*, 280, 269

Kaastra, J. S., Mewe, R., Liedahl, D. A., Singh, K. P., White, N. E., & Drake, S. A. 1996, *A&A*, 314, 547

Kaastra, J. S. & Mewe, R. 1993, *A&AS*, 97, 443

Kinkhabwala, A. et al. 2002, *ApJ*, 575, 732

Klapisch, M., Schwab, J. L., Fraenkel, J. S., & Oreg, J. 1977, *Opt. Soc. Am.*, 61, 148

Krolik, J. H., McKee, C. F., & Tarter, C. B. 1981, *ApJ*, 249, 422

Liedahl, D. A. & Paerels, F. 1996, *ApJ*, 468, L33

Liedahl, D. A. 1999, in *X-ray Spectroscopy in Astrophysics*, EADN School proceedings, ed. J. A. van Paradijs, & J. A. M. Bleeker (Amsterdam: Springer), 189

Mewe, R. & Schrijver, J. 1978, *A&A*, 65, 99

Palmeri, P., Mendoza, C., Kallman, T. R., Bautista, M. A., & Meléndez, M. 2003, *A&A*, 410, 359

Petterson, J. A. 1975, *ApJ*, 201, L61

Petterson, J. A., Rothschild, R. E., & Gruber, D. E. 1991, *ApJ*, 378, 696

Podsiadlowski, P., Rappaport, S., & Pfahl, E. D. 2002, *ApJ*, 565, 1107

Porquet, D. & Dubau, J. 2000, *A&AS*, 143, 495

Ramsay G., Zane S., Jimenez-Garate M., den Herder J., & Hailey C., 2001, *MNRAS*, submitted

Raymond, J. C. 1993, *ApJ*, 412, 267

Reynolds, A. P., Quaintrell, H., Still, M. D., Roche, P., Chakrabarty, D., & Levine, S. E. 1997, *MNRAS*, 288, 43

Sako, M. 2003, *ApJ*, 594, 1108

Sako, M., Liedahl, D. A., Kahn, S. M., & Paerels, F. 1999, *ApJ*, 525, 921

Scargle, J. D. in *Statistical Challenges in Modern Astronomy (SCMA III)*, ed. E. D. Feigelson, G. J. Babu (New York: Springer), 293

Schaller, G., Schaerer, D., Meynet, G., & Maeder, A. 1992, *A&AS*, 96, 269

Scott, D. M. & Leahy, D. A. 1999, *ApJ*, 510, 974

Scott, D. M., Leahy, D. A., & Wilson, R. B. 2000, *ApJ*, 539, 392

Tananbaum, H., Gursky, H., Kellogg, E. M., Levinson, R., Schreier, E., & Giacconi, R. 1972, *ApJ*, 174, L143

White, N. E. & Angelini, L. 2001, *ApJ*, 561, L101

White, N. E., Nagase, F., Parmar, A. N. 1995, "The properties of X-ray binaries", pp. 1-57, eds. Lewin, H. G., Jan Van Paradijs, Van Der Heuvel, E. P., "X-ray Binaries", 1995 (Cambridge University Press).

Wilms, J., Allen, A., & McCray, R. 2000, *ApJ*, 542, 914

Wilson, R. B., Scott, D. M., & Finger, M. H. 1997, *AIP Conf. Proc.* 410, *Proceedings of the Fourth Compton Symposium*, ed. C. D. Dermer, M. S. Strickman, & J. D. Kurfess (New York: AIP Press), 739

Wojdowski, P. S., Liedahl, D. A., Sako, M., Kahn, S. M., & Paerels, F. 2003, *ApJ*, 582, 959

Zane, S., Ramsay, G., Jimenez-Garate, M. A., Willem den Herder, J., & Hailey, C. J. 2004, MNRAS, 350, 506

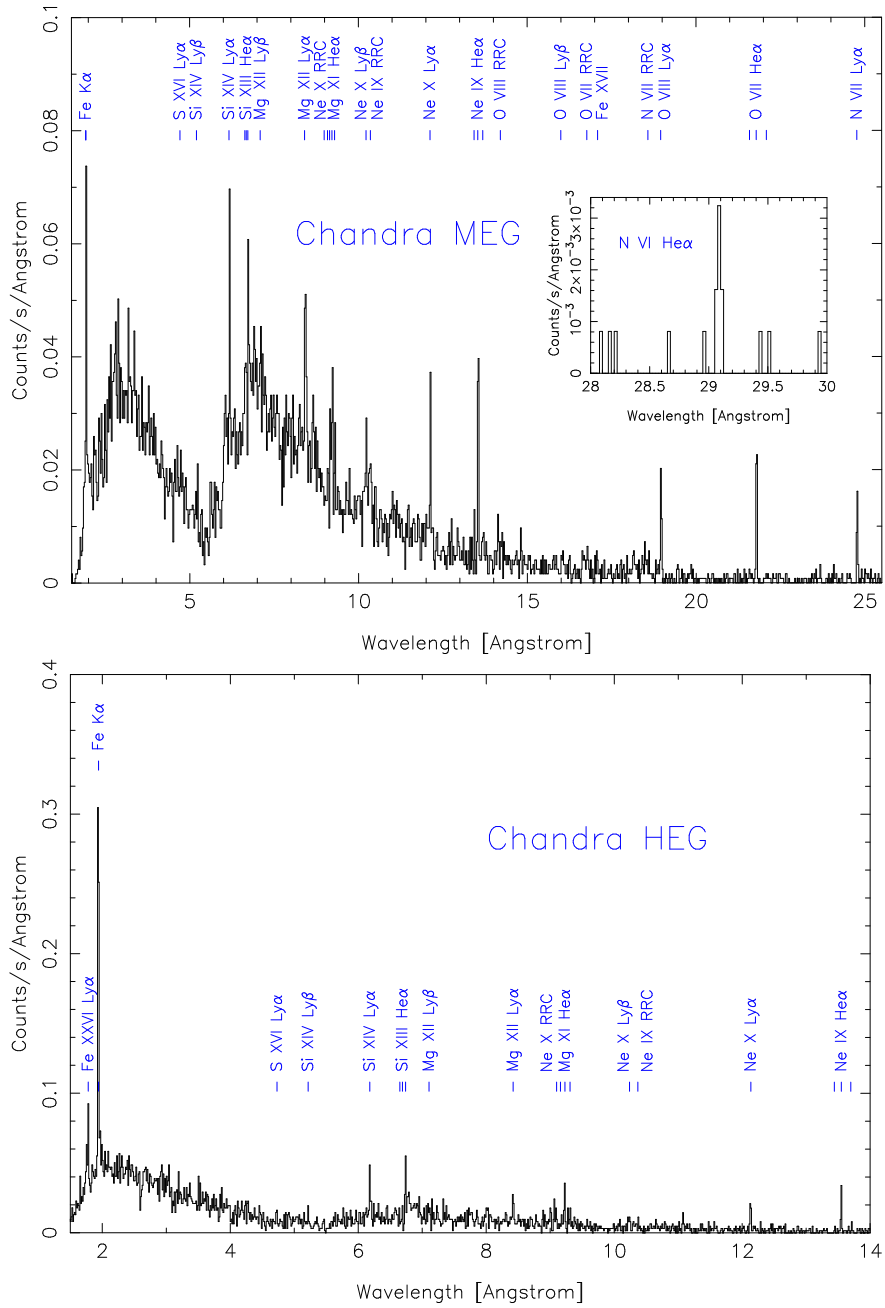


Fig. 1.— The MEG and HEG count spectra of Hercules X-1 during its low-state shows numerous radiative recombination lines and continua, a strong Fe K α fluorescence line, and a continuum which may be produced by Compton scattering. The large range of temperatures at which these emission lines originate is a direct probe of the ionization structure of the upper layers of the accretion disk atmosphere and corona.

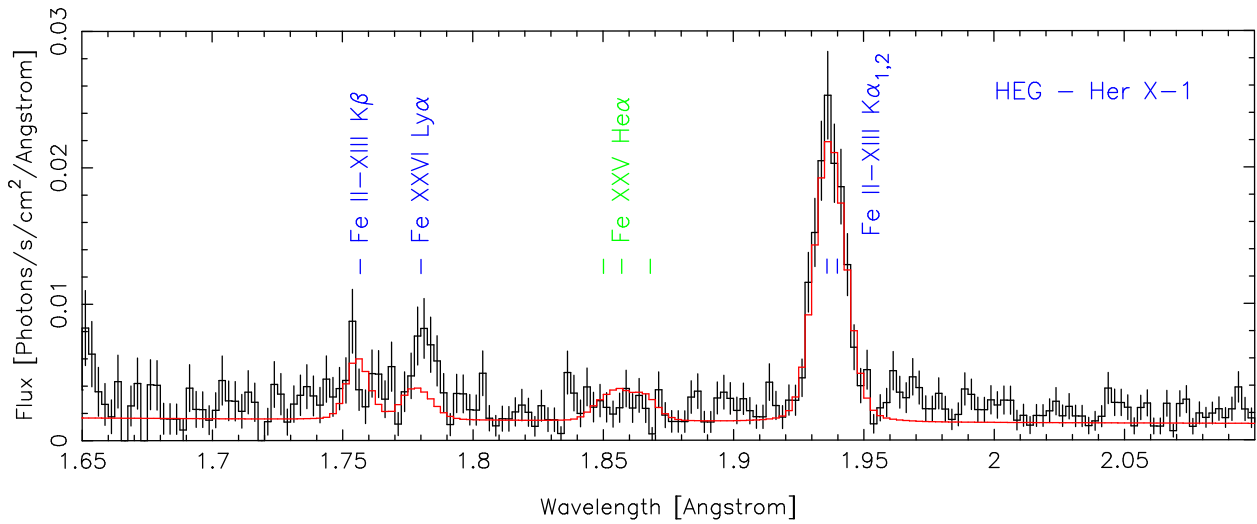


Fig. 2.— HEG spectrum, showing both Fe I-Fe XIII K α and K β fluorescence lines, as well as the Fe XXVI Ly α radiative recombination line. The disk corona and atmosphere model is over-plotted in red, except for the fluorescence lines, which were fit independently. The green label indicates that the line was produced in the model but not detected.

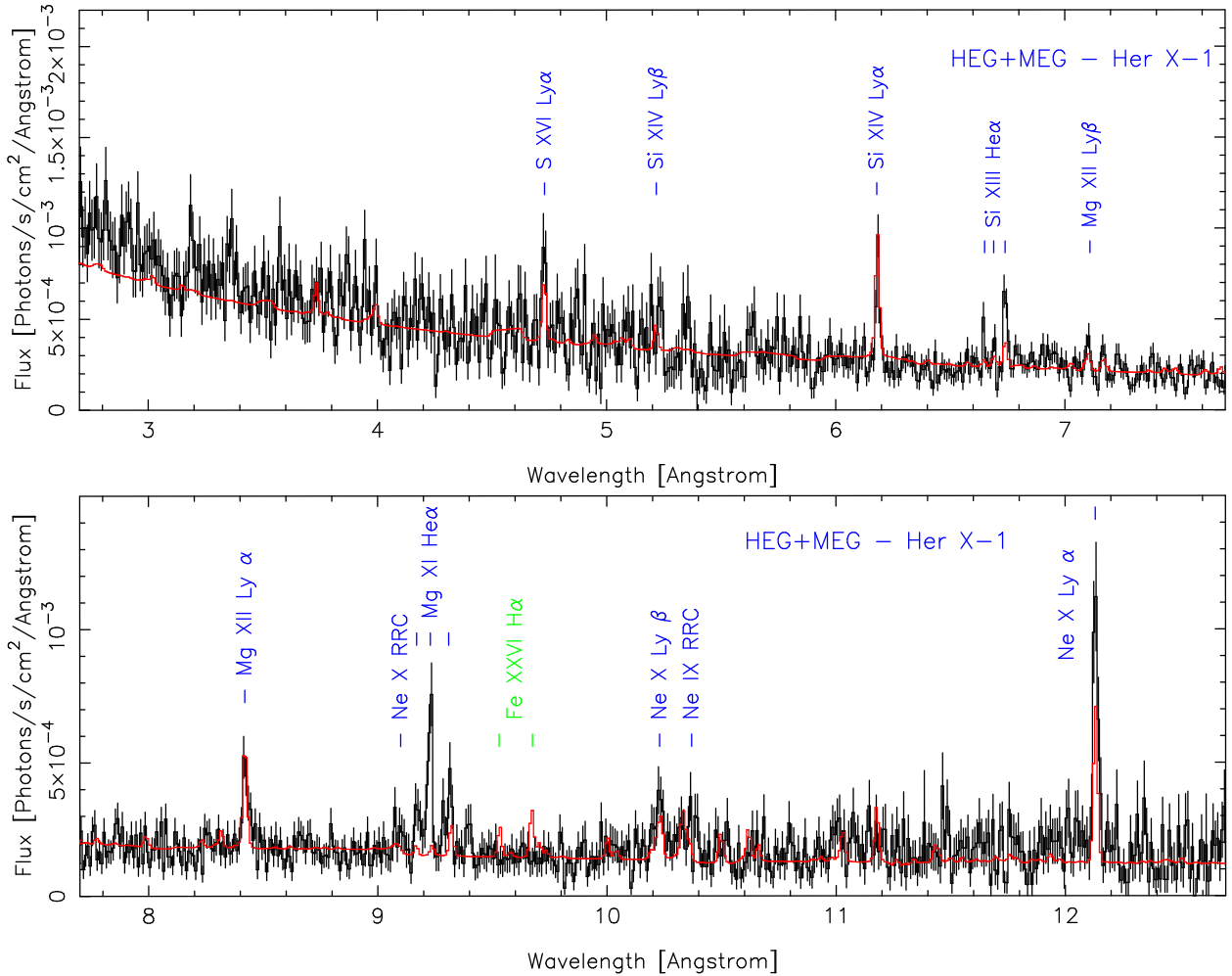


Fig. 3.— Added HEG and MEG spectra. The disk corona and atmosphere model is over-plotted in red. The green label indicates that the line was produced in the model but not detected.

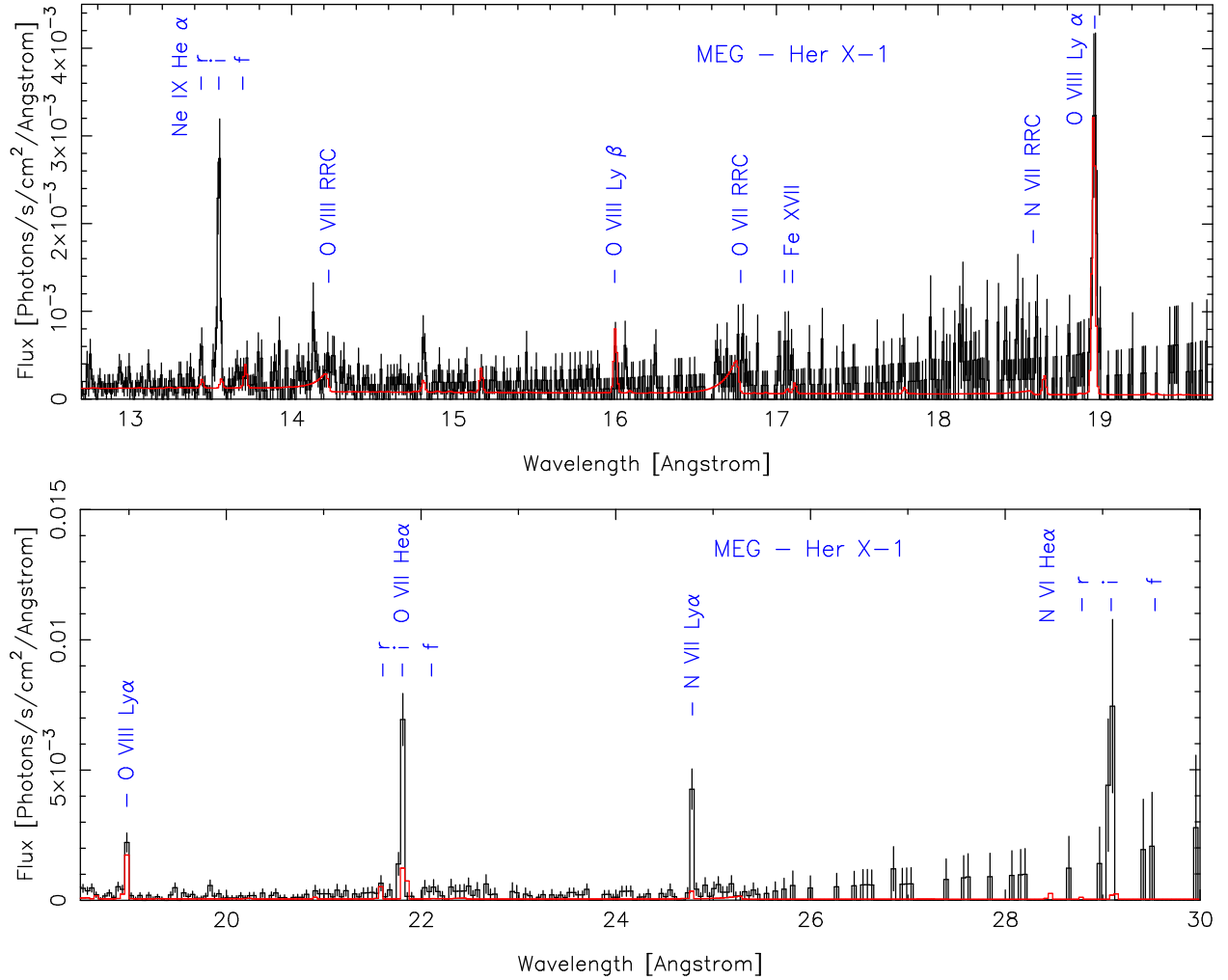


Fig. 4.— MEG spectra which show that the nitrogen lines are quite bright relative to the oxygen lines, as observed with *XMM-Newton* (Jimenez-Garate et al. 2002). The disk corona and atmosphere model is shown in red.

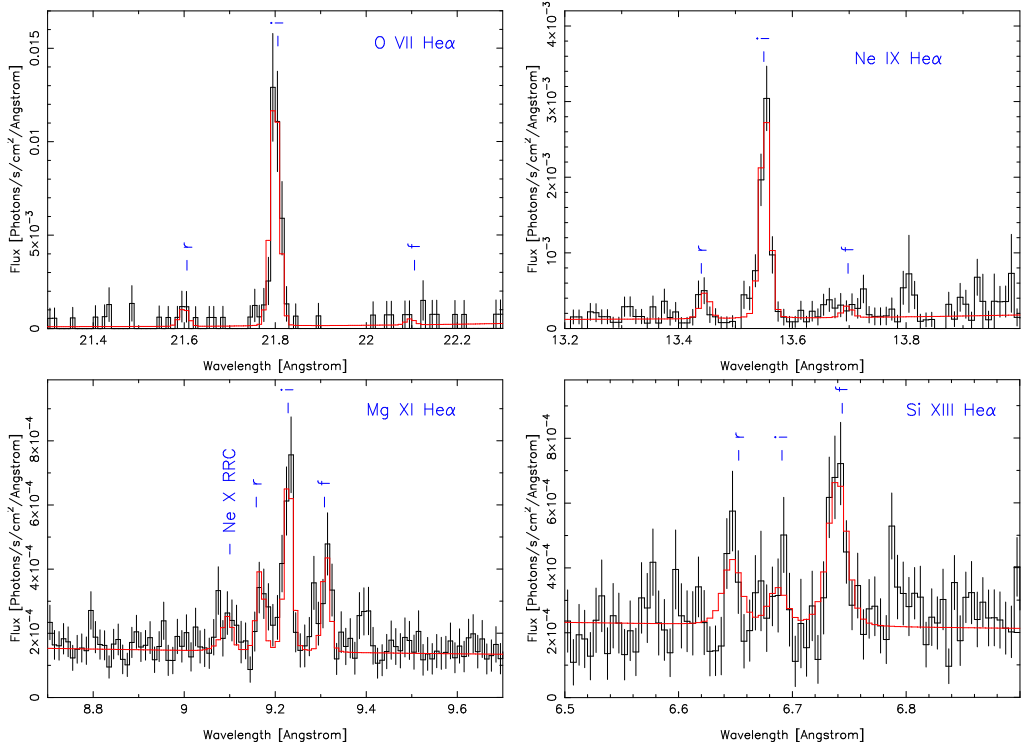


Fig. 5.— He-like triplet lines for O VII, Ne IX, Mg XI, and Si XIII. The line ratios evolve smoothly from O VII and Ne IX with $R \sim 0$, to Si XIII with $R = 3 \pm 1$. The R ratio of Mg XI has a critical value $R = 0.51 \pm 0.12$, which can provide a precise measure of the density. The Gaussian line fits (not from the disk model) are over-plotted in red.

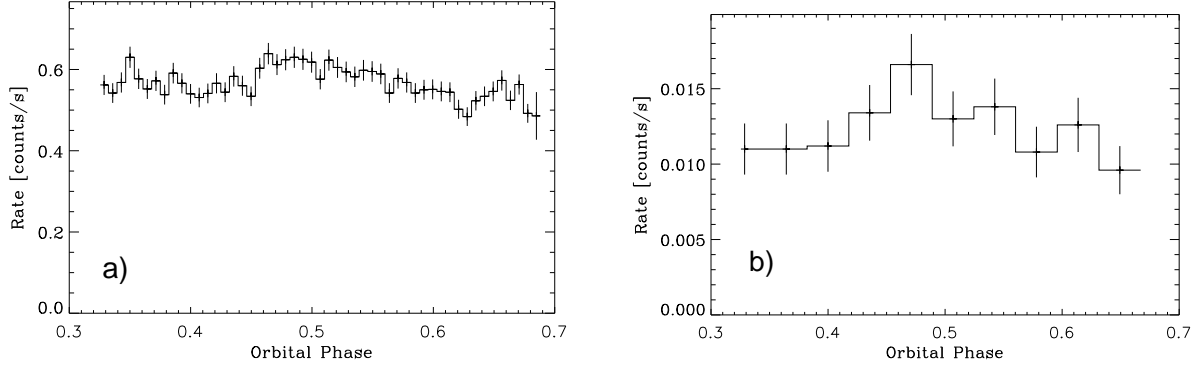


Fig. 6.— Light curves of: *a*) the total HETGS dispersed count rate with $\lambda > 1.5 \text{ \AA}$, and *b*) the Fe I-Fe XIII K α line HETGS count rate. The orbital period is 1.7 days.

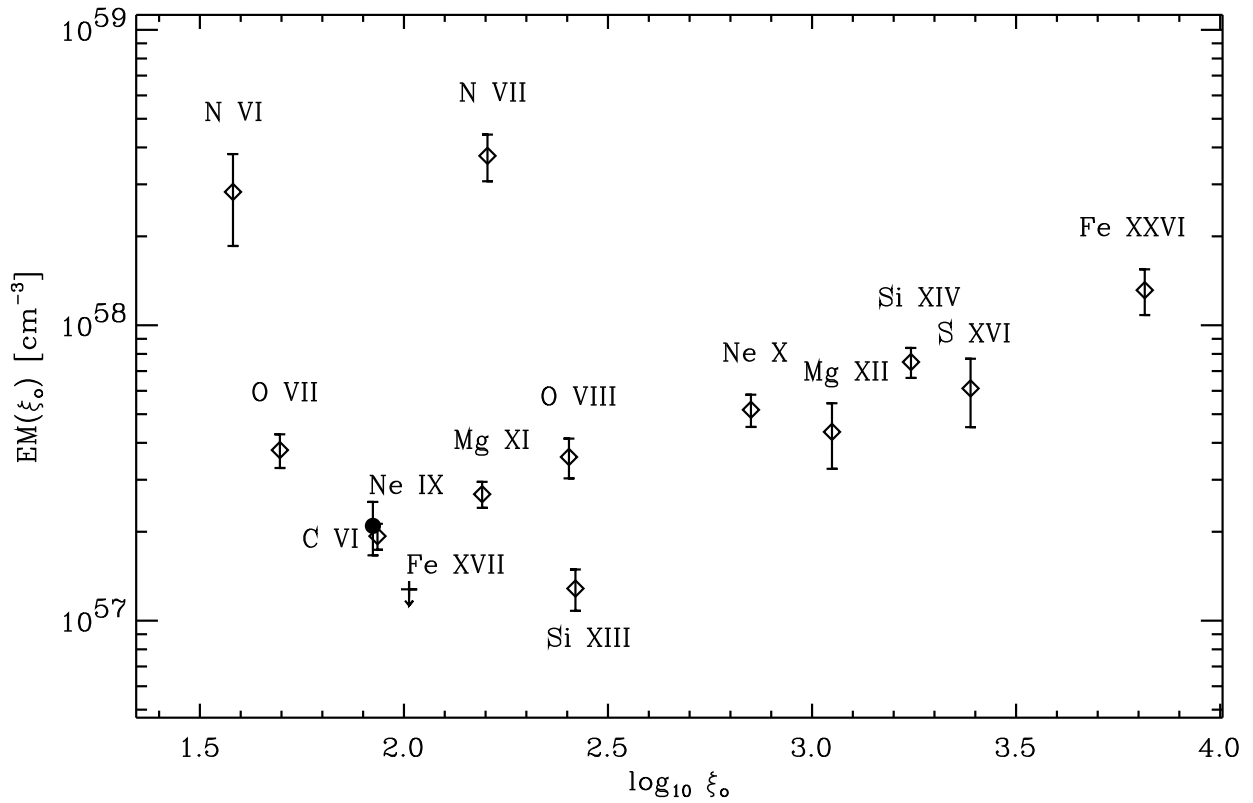


Fig. 7.— Estimated emission measure (EM) at a single ionization parameter of formation ξ_o , derived from the HETGS line fluxes (diamonds) and from the C VI flux measured with RGS (Jimenez-Garate et al. 2002, filled circle). Both N VII and N VI indicate an excess nitrogen abundance. This rough estimate of the EM has the virtue of being insensitive to thermal instabilities. We assume a charge state fraction $f_{i+1} = 0.25$ for the recombining ions.

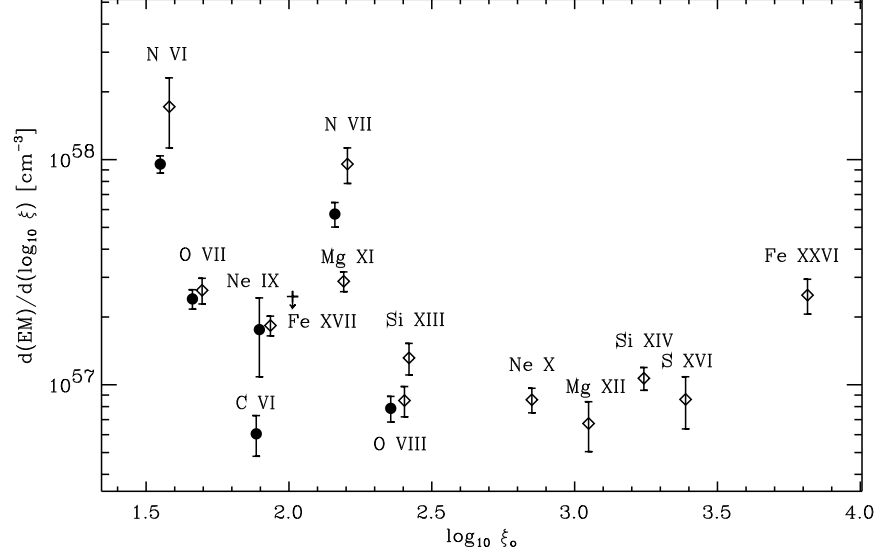


Fig. 8.— Differential emission measure (DEM) vs. ionization parameter. The line fluxes measured with HETGS (diamonds) are complemented with the fluxes from *XMM-Newton* RGS (Jimenez-Garate et al. 2002, filled circles). This is more accurate than Fig. 7 because the DEM is calculated in a grid spanning the full ξ range. However, it is also sensitive to the thermal and ionization balance solution from XSTAR (Kallman & McCray 1982), as well as the DEM slope. The over-abundance of N and depletion of C is observed. The predicted thermal instability regime occurs at $1.9 < \log_{10} \xi < 2.4$. The excess DEM for the He-like ions in this regime suggests that the plasma is more stable than predicted.

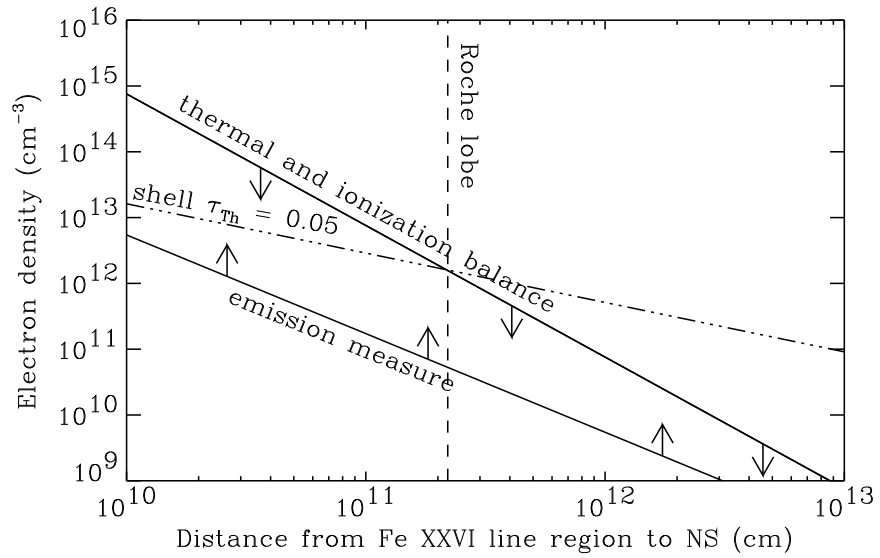


Fig. 9.— Density limits derived for the Fe XXVI emission region, versus its maximum distance (r) to the neutron star. The Thomson depth is plotted for a spherical shell with $r_{\min} = r/3$ and $r_{\max} = r$.

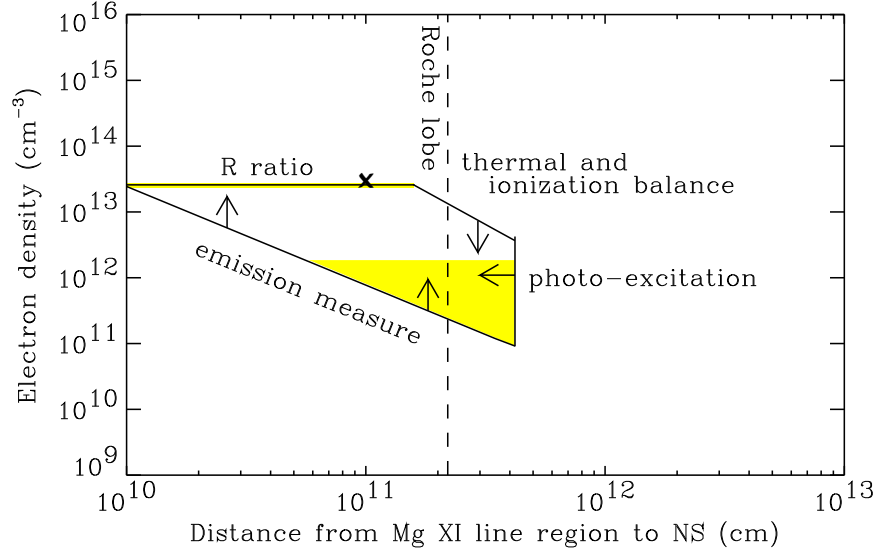


Fig. 10.— Limits on the density of the Mg XI emission region, versus its maximum distance to the neutron star. The R ratio strongly limits the plasma to be close to the density and photoexcitation boundary. The irradiated disk atmosphere model prediction is shown by an **X**, and the thermally stable density regimes in that model are shaded in yellow.

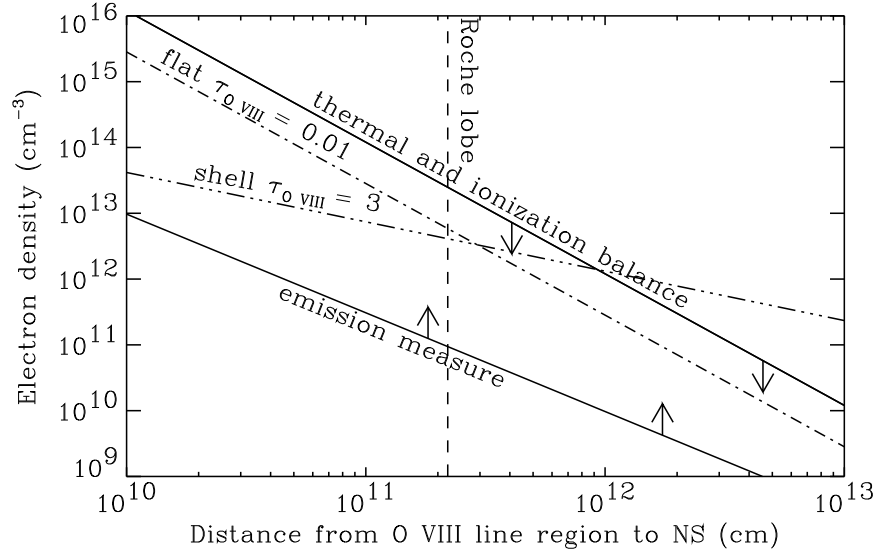


Fig. 11.— Limits on the density of the O VIII emission region, versus its maximum distance to the neutron star. The velocity broadening suggests that the emission region should be close to the Roche Lobe of the neutron star. The O VIII edge optical depths for two geometries are shown: for a filled spherical shell with $r_{\min} = r/3$ and $r_{\max} = r$ ("shell"), and for a face-on flattened disk geometry ("flat").

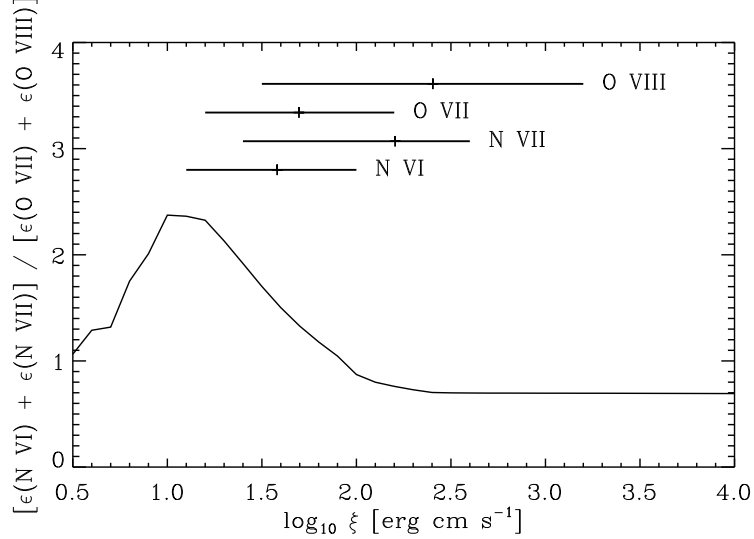


Fig. 12.— Line emissivity ratio (E) built from the N VI, N VII, O VII, and O VIII line emissivities obtained from the XSTAR and HULLAC models, as a function of ionization parameter $\log_{10} \xi$. The observed line ratio will differ from this emissivity ratio by a factor of A_N/A_O , the ratio of elemental abundances. At the top of the figure, we show the $\log_{10} \xi$ range at which the line emissivities are $> 20\%$ of the peak emissivity, with the $\log_{10} \xi_o$ of formation (peak emissivity) marked.

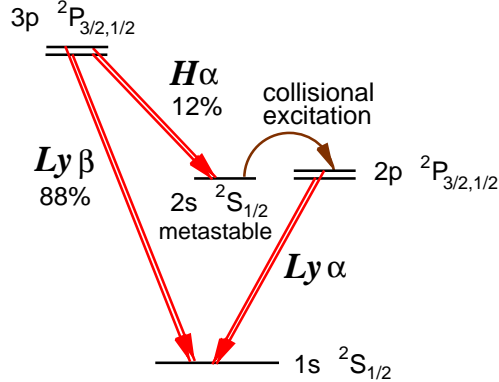


Fig. 13.— Abridged energy level diagram for a H-like ion, showing the decay channels of the $3p\ ^2P_{3/2,1/2}$ levels. These channels show how a Ly β photon gets scattered or converted to other photons. Once a Ly β photon is absorbed, there is an 88% probability for an electron at either of the $3p\ ^2P_{3/2,1/2}$ levels to re-emit a Ly β photon, resulting in a resonant scattering event. Alternatively, there is a 12% probability for the same initial states to decay by emission of an H α photon. Once an H α is emitted, the metastable $2s\ ^2S_{1/2}$ level decays to the ground state via two photons (not shown), unless the electron density is above a critical threshold n_{crit} . For $n_e > n_{\text{crit}}$, the $2s\ ^2S_{1/2}$ level gets excited to $2p\ ^2P_{3/2}$, and a Ly α photon is emitted. The photons shown in the figure are all unresolved doublets.

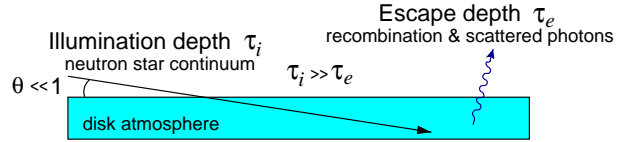


Fig. 14.— In an accretion disk atmosphere which is illuminated with $\theta \ll 1$, two optical depths are relevant. In the Her X-1 spectrum, recombination emission dominates over resonance scattering, implying that $\tau_i \gtrsim 100$ for the He-like ion r lines. The mean number of scatterings and any line destruction are sensitive to τ_e . The X-ray Bowen fluorescence effect is excluded because $\langle N \rangle \lesssim 69$ and thus $\tau_e \lesssim 99$ for O VIII Ly α_1 . The measured τ are beginning to show that the emission region is elongated.

Table 1. X-ray Emission Features and Disk Atmosphere Model Predictions

Line(s)	λ [Å] ^a	$(\Delta v)_\sigma$ [km/s]	Observed Flux ^b	Model Flux ^b (λ)
N VI <i>i</i>	29.08	...	64 ± 22	1.9
N VII Ly α	24.78	...	25 ± 4.5	2.0
O VII <i>f</i>	22.10	...	1.2 ± 1.2 (< 3.9)	0.36
O VII <i>i</i>	21.800 ± 0.006	< 110	40.5 ± 5.5	9.2
O VII <i>r</i>	21.60	...	3.1 ± 1.6	2.5
O VIII Ly α	18.970 ± 0.006	< 270	13 ± 2	9.0
N VII RRC	18.59	...	18 ± 5	0.63
Fe XVII	17.05, 17.10	...	< 3.8	0.56
O VII RRC	16.78	...	2.5 ± 1.0	4.2
O VIII Ly β	16.01	...	0.85 ± 0.30	2.0
O VIII RRC	14.23	...	5.8 ± 1.2	2.4
Ne IX <i>f</i>	13.70	...	0.17 ± 0.17 (< 0.96)	1.4
Ne IX <i>i</i>	13.553 ± 0.003	< 160	7.3 ± 0.75	0.71
Ne IX <i>r</i>	13.45	...	0.87 ± 0.33	0.66
Ne X Ly α	12.135 ± 0.003	< 240	3.2 ± 0.4	1.8
Ne IX RRC	10.37	...	1.82 ± 0.36	0.80
Ne X Ly β	10.24	...	0.59 ± 0.16	0.67
Fe XXVI H α	9.53, 9.67	...	< 0.24	0.79
Mg XI <i>f</i>	9.31	...	0.84 ± 0.17	0.32
Mg XI <i>i</i>	9.229 ± 0.003	< 380	1.65 ± 0.21	0.14
Mg XI <i>r</i>	9.17	...	0.59 ± 0.15	0.10
Ne X RRC	9.10	...	0.73 ± 0.19	0.32
Mg XII Ly α	8.417 ± 0.003	...	1.12 ± 0.28	1.1
Mg XII Ly β	7.11	...	0.42 ± 0.11	0.30
Si XIII <i>f</i>	6.74	...	1.08 ± 0.15	.38
Si XIII <i>i</i>	6.69	...	0.36 ± 0.12	.18
Si XIII <i>r</i>	6.647 ± 0.003	...	0.54 ± 0.13	.11
Si XIV Ly α	6.185 ± 0.003	< 340	1.44 ± 0.23	1.8
Si XIV Ly β	5.22	...	0.61 ± 0.26	0.35
S XVI Ly α	4.73	...	1.19 ± 0.31	0.88
Fe II–XIII K α_2	1.940 ± 0.003^c	< 680	10.61 ± 1.84	...
Fe II–XIII K α_1	1.936 ± 0.003^c	< 680	22.00 ± 1.94	...
Fe XXVI Ly α	1.78	...	7.37 ± 1.30	1.9
Fe II–XIII K β	1.76	...	5.10 ± 1.20	...

Note. — The model corresponds to an accretion disk atmosphere and corona. The statistical errors and upper limits are given to 66 % confidence, except for the upper limits, which are 90 % confidence. Symbols: λ = line wavelength; $(\Delta v)_\sigma$ = standard deviation of the Gaussian emission line. We include systematics in the measurements, except for the line fluxes. We compare the data to the disk atmosphere and corona model.

^aWeak features are assigned nominal wavelengths. Otherwise, the measured wavelengths are shown with error bars. The nominal wavelengths are rounded up to 0.01 mÅ.

^bIn units of 10^{-5} photons cm $^{-2}$ s $^{-1}$.

^cThis is the relative shift of the Fe K α pair with wavelength and flux ratios tied.

Table 2: Continuum fit parameters

Component (Model)	Parameter (Unit)	Value
Absorption (1)	N_H (10^{18} cm $^{-2}$)	13 (fixed)
Power-law (1)	Norm. at 1 keV (phot keV $^{-1}$ cm $^{-2}$ s $^{-1}$)	$(9.6 \pm 0.4) \times 10^{-4}$
Power-law (1)	Photon Index	0.27 ± 0.03
Blackbody (1)	Norm. (10^{39} erg s $^{-1}$ / (10 kpc) 2)	$(3.5 \pm 0.2) \times 10^{-5}$
Blackbody (1)	Temperature (keV)	0.181 ± 0.015
(1)	χ^2 /DOF	1292/1844 = 0.70
Absorption (2)	N_H (10^{18} cm $^{-2}$)	13 (fixed)
Power-law (2)	Norm. at 1 keV (phot keV $^{-1}$ cm $^{-2}$ s $^{-1}$)	$(1.34 \pm 0.01) \times 10^{-3}$
Power-law (2)	Photon Index	0.53 ± 0.01
(2)	χ^2 /DOF	1703/1844 = 0.92

Note. — DOF = degrees of freedom.

Table 3: Helium-like line diagnostics and photoexcitation of the $1s2s$ 3S_1 level

Ion	$R = f/i$ Line Ratio	$G = (f+i)/r$ Line Ratio	$\lambda_{f \rightarrow i}$ (Å) ⁽¹⁾	Flux $F_{\lambda_{f \rightarrow i}}$ (10^{-13} erg cm $^{-2}$ s $^{-1}$ Å $^{-1}$)	$2\ 3S_1 \rightarrow 1\ ^1S_0$ Rate (s $^{-1}$) ^(2,5)	$w_{f \rightarrow i}(r=10^{11}$ cm) Rate (s $^{-1}$)	d Radius (cm)	n_e Density (cm $^{-3}$)
Si XIII	3.0 ± 1.0	2.7 ± 0.7	864	$\sim 1.1^{(4)}$	3.56×10^5	7×10^4	$> 8 \times 10^{10}$	$< 5 \times 10^{12}$
Mg XI	0.51 ± 0.12	4.2 ± 1.2	1033	$\sim 3.1^{(4)}$	7.24×10^4	4×10^5	2×10^{11}	$(2 \pm 1) \times 10^{13}$
Ne IX	< 0.13	8.6 ± 3.4	1270	$1.9 \pm 0.1^{(3)}$	1.09×10^4	5×10^5	$< 6 \times 10^{11}$	$> 1 \times 10^{13}$
O VII	< 0.10	13 ± 7	1637	$1.5 \pm 0.2^{(3)}$	1.04×10^3	1×10^6	$< 3 \times 10^{12}$	$> 8 \times 10^{11}$

Note. — The statistical errors are calculated to 66% confidence and the limits to 90%. Symbols: $\lambda_{f \rightarrow i}$ = wavelengths of $1s2s$ $^3S_1 \rightarrow 1s2p$ $^3P_{0,1,2}$ transitions; w_f = radiative decay rates for $1s2p$ $^3S_1 \rightarrow 1s^2$ 1S_0 ; $w_{f \rightarrow i}$ = calculated photoexcitation rate for $1s2p$ $^3S_1 \rightarrow 1s2p$ $^3P_{0,1,2}$. The energy level notation is abridged in the table header.

References. — (1) Porquet et al. 2001; (2) Drake 1971; (3) from the *Hubble GHRS* at $\phi = 0.56$ –0.60 by Boroson et al. 1996; (4) Boroson et al. 2001, and private communication 2003, FUSE data near $\phi = 0.5$; (5) From HULLAC atomic code, Klapisch et al. (1977).

Table 4. Ly α to Ly β Line Ratios

Ion	kT_o [eV]	Ly α /Ly β theory	Ly α /Ly β observed
O VIII	disk	4.7	15 ± 6
	25	4.9	
Ne X	disk	3.3	5.4 ± 1.6
	90	4.6	
Mg XII	disk	4.8	2.7 ± 1.0
	154	4.8	
Si XIV	disk	5.5	2.4 ± 1.1
	237	4.8	

Note. — The theoretical values were calculated with HULLAC in the optically thin limit at the temperature of peak emission, and for the disk atmosphere (with temperatures $2 < kT < 860$ eV), which includes possible line blends with other species. T_o = average temperature weighted by the emissivity of the RR line ($f_{i+1} S_{ul}$).

Table 5. RRC to Radiative Recombination (RR) Line Ratios

Ion	kT_o [eV]	RRC/RR theory	RRC/RR observed
N VI	2.8	0.24	...
	disk	0.26	
N VII	14	0.83	$0.72 \pm 0.25, 0.28 \pm 0.14^{(1)}$
	disk	0.32	
O VII	3.5	0.32	0.06 ± 0.02
	disk	0.35	
O VIII	25	0.87	0.45 ± 0.12
	disk	0.27	
Ne IX	6.5	0.25	0.22 ± 0.05
	disk	0.29	
Ne X	90	1.02	0.23 ± 0.07
	disk	0.18	

Note. — The theoretical values were calculated with HULLAC in the optically thin limit. For RR, we use either Ly α or He α , corresponding to each H-like or He-like ion, respectively. T_o = average temperature weighted by the emissivity of the RR line. The disk model temperature range is $2 < kT < 860$ eV.

References. — (1) Jimenez-Garate et al. (2001).